CLASSIFICATION OF HISTOPATHOLOGICAL CANCER STEM CELL IMAGES IN H&E STAINED LIVER TISSUES

A THESIS SUBMITTED TO

THE GRADUATE SCHOOL OF ENGINEERING AND SCIENCE

OF BILKENT UNIVERSITY

IN PARTIAL FULFILLMENT OF THE REQUIREMENTS FOR

THE DEGREE OF

MASTER OF SCIENCE

IN

ELECTRICAL AND ELECTRONICS ENGINEERING

By

Cem Emre Akbaş

March 2016

CLASSIFICATION OF HISTOPATHOLOGICAL CANCER STEM CELL IMAGES IN H&E STAINED LIVER TISSUES

By Cem Emre Akbaş

March 2016

We certify that we have read this thesis and that in our opinion it is fully adequate, in scope and in quality, as a thesis for the degree of Master of Science.

A. Enis Çetin(Advisor)

Uğur Güdükbay

Kasım Taşdemir

Approved for the Graduate School of Engineering and Science:

Levent Onural
Director of the Graduate School

ABSTRACT

CLASSIFICATION OF HISTOPATHOLOGICAL CANCER STEM CELL IMAGES IN H&E STAINED LIVER TISSUES

Cem Emre Akbaş
M.S. in Electrical and Electronics Engineering
Advisor: A. Enis Çetin
March 2016

Microscopic images are an essential part of cancer diagnosis process in modern medicine. However, diagnosing tissues under microscope is a time-consuming task for pathologists. There is also a significant variation in pathologists' decisions on tissue labeling. In this study, we developed a computer-aided diagnosis (CAD) system that classifies and grades H&E stained liver tissue images for pathologists in order to speed up the cancer diagnosis process. This system is designed for H&E stained tissues, because it is cheaper than the conventional CD13 stain.

The first step is labeling the tissue images for classification purposes. CD13 stained tissue images are used to construct ground truth labels, because in H&E stained tissues cancer stem cells (CSC) cannot be observed by naked eye.

Feature extraction is the next step. Since CSCs cannot be observed by naked eye in H&E stained tissues, we need to extract distinguishing texture features. For this purpose, 20 features are chosen from nine different color spaces. These features are fed into a modified version of Principal Component Analysis (PCA) algorithm, which is proposed in this thesis. This algorithm takes covariance matrices of feature matrices of images instead of pixel values of images as input. Images are compared in the eigenspace and classifies them according to the angle between them. It is experimentally shown that this algorithm can achieve 76.0% image classification accuracy in H&E stained liver tissues for a three-class classification problem.

Scale invariant feature transform (SIFT), local binary patterns (LBP) and directional feature extraction algorithms are also utilized to classify and grade H&E stained liver tissues. It is observed in the experiments that these features

do not provide meaningful information to grade H&E stained liver tissue images.

Since our aim is to speed up the cancer diagnosis process, computationally efficient versions of proposed modified PCA algorithm are also proposed. Multiplication-free cosine-like similarity measures are employed in the modified PCA algorithm and it is shown that some versions of the multiplication-free similarity measure based modified PCA algorithm produces better classification accuracies than the standard modified PCA algorithm. One of the proposed multiplication-free similarity measures achieves 76.0% classification accuracy in our dataset containing 454 images of three classes.

Keywords: PCA, Tissue Grading, Texture Classification, Image Classification.

ÖZET

H&E BOYANMIŞ KARACİĞER DOKULARINDA HİŞTOPATOLOJİK KANSER KÖK HÜCRE İMGELERİNİN SINIFLANDIRILMASI

Cem Emre Akbaş
Elektrik-Elektronik Mühendisliği, Yüksek Lisans
Tez Danışmanı: A. Enis Çetin
Mart 2016

Mikroskopik görüntüler modern tıpta kanser tanısının önemli bir parçasıdır. Fakat, dokulara mikroskop altında tanı koymak patologlar için oldukça zaman alıcı ve yorucu bir iştir. Bu tezde, pataloglar için kanser tanı sistemini hızlandırma amacıyla H&E boyanmış doku imgelerini sınıflandıran ve derecelendiren bilgisayar yardımlı bir tanı sistemi geliştirdik. Bu sistem H&E boyanmış dokular için dizayn edildi, çünkü bu boya yaygın olarak kullanılan CD13 boyasından daha düşük maliyetlidir.

Bu sistemimizde ilk adım doku imgelerinin etiketlenmesidir. CD13 boyanmış imgeler yer gerçekliği etiketlerinin oluşturulması için kullanılmıştır, çünkü H&E boyanmış dokularda kanser kök hücreleri çıplak gözle (KKH) görülememektedir.

Sistemimizdeki sonraki adım öznitelik çıkarımıdır. KKH'ler H&E boyanmış dokularda çıplak gözle görülemediği için örüntü ayırt edici öznitelikler çıkarmamız gerekmektedir. Bu amaçla dokuz farklı renk uzayından 20 öznitelik seçilmiştir. Bu öznitelikler, bu çalışmada önerilen değiştirilmiş Ana Bileşenler Analizi (PCA) algoritmasına girdi olarak verilmiştir. Bu algoritma, imgelerin piksel değerleri yerine imgelerin öznitelik matrislerinin ortak değişinti matrislerini girdi olarak kullanır. mgeler özuzayda (eigenspace) karşılaştırır ve aralarındaki açıya göre sınıflandırılır. Bu algoritmanın üç sınıf H&E boyanmış karaciğer dokularını sınıflandırma probleminde 76.0% imge sınıflandırma başarısı sağladığı deneysel sonuçlarla gösterilmiştir.

Öznitelik çıkarmak için ölçekten bağımsız öznitelik dönüşümü (SIFT), yerel ikili örüntüler (LBP) ve yönsel öznitelik çıkarma algoritmalarından da faydalanılmıştır. Deneylerde, bu öznitelik çıkarma algoritmalarının H&E boyanmış

karaciğer doku imgelerinin derecelendirilmesi için anlamlı bilgi sağlayamadığı görülmüştür.

Bu çalışmada amacımız kanser tanı sürecini hızlandırmak olduğu için, değiştirilmiş PCA algoritmasının hesap yükü düşürülmüş versiyonları da önerilmiştir. Çarpmasız kosinüs benzeri benzerlik ölçüleri değiştirilmiş PCA algoritmasında kullanılmıştır ve çarpmasız benzerlik ölçüsü tabanlı değiştirilmiş PCA algoritmalarının bazılarının çarpmaya dayalı standart değiştirilmiş PCA algoritmasından daha iyi sınıflandırma sonuçları ürettiği görülmüştür. Önerilen çarpmasız benzerlik ölçülerinden birisi değiştirilmiş PCA algoritmasında kullanıldığında üç sınıfa ait 454 imge içeren bir veri setinde %76.0 sınıflandırma başarısı elde edilmiştir.

Anahtar sözcükler: PCA, Doku Derecelendirme, Örüntü Sınıflandırma, Görüntü Sınıflandırma.

"Simplicity is the ultimate sophistication."

- Leonardo da Vinci

Dedicated to my dearest grandfather Ali Yurtsever...

Acknowledgement

My first and foremost thanks goes to my family. None of this would have happened without them and I am deeply indebted for their continuous and unconditional support. Besides all, they also took major parts in my life-long learning process:

- My mother taught me how to read at the age of three and initiated my learning journey.
- My brother helped me establish a solid analytical thinking background.
- My father introduced me modern science and molecular biology at my early ages.

I would also like to express my deepest gratitude to:

- My thesis advisor Dr. Ahmet Enis Çetin for sharing his invaluable academic and life experiences with me.
- My thesis committee members Dr. Uğur Güdükbay and Dr. Kasım Taşdemir for their valuable feedback.
- TÜBİTAK for the scholarship. This thesis is partially funded by TÜBİTAK 113E069 and TÜBİTAK 213E032 project.
- Dr. Ece Akhan Güzelcan and Dr. Rengül Çetin Atalay for providing CD13 and H&E stained liver and lung tissue image datasets.
- Dr. Kasım Taşdemir for sharing his precious research experience with me and for his contributions to my research.
- My close friend Erdem Karagül for magically appearing at 'that' moments.
- My close friend Hazal Demiral for having visionary answers for all my hardest questions and Oxygen-filled breaks.

- My close friend Okan Demir for enlightening coffee talks mostly at the toughest moments of the graduate life.
- My close friends Sinem Meleknur Sertel, Alican Bozkurt, Fırat Yılmaz, Altuğ Baykal, Eren Halaç, Gökmen Can, Bilgehan Işıklı, Alper Yoğurt, Mustafa Ütkür, Egemen Özdamar, Ekrem Bilgehan Uyar and Yaşar Daysal for their support and good memories.
- Past and present members of Bilkent Signal Processing Group: Alican Bozkurt, Mohammad Tofighi, Hüseyin Aslanoğlu, Onur Yorulmaz, Oğuzhan Oğuz, Musa Tunç Arslan and Rasim Akın Sevimli.
- Mirco de Govia for his inspirational tunes. The support of his music was quite exceptional.
- Alican Bozkurt (again) for everything.

The story goes that Picasso was sitting in a Paris café when an admirer approached and asked if he would do a quick sketch on a paper napkin. Picasso politely agreed, swiftly executed the work and handed back the napkin, but not before asking for a rather significant amount of money. The admirer was shocked: "How can you ask for so much? It took you five minutes to draw this!" "No", Picasso replied, "It took me 40 years plus five minutes". Of course, it took me 24.5 years plus 9 months to develop my research background and produce this thesis. All my previous teachers, classmates and friends who took part in my learning journey deserve my final thanks.

Contents

List of Figures

List of Tables

Chapter 1

Introduction

In cancer diagnosis and grading process, analysis of microscopic images is still the most reliable method. However, grading liver tissue images under microscope is a time-consuming and tiring task. There is also a significant variation in pathologists' decisions on tissue labeling [1–4]. Therefore, there may occur human-based errors due to tiredness. Our main motivation to develop a computer-aided diagnosis (CAD) system is to speed up the cancer diagnosis process, since time is a very critical issue in cancer diagnosis and treatment. Another important advantage of using a CAD is that its grading and classification results are reproducible.

CAD enables us to have a two stage decision mechanism. First, our algorithm makes a decision. Then, the pathologist checks our algorithm's decision and makes the final decision. This two stage decision mechanism help the pathologist make more correct decisions about the cancer diagnosis and tissue grading.

In the early 1990's, digital mammography was one of the first developed CAD system [5, 6]. Since that day, CAD has been actively used in detection of breast cancer in the United States of America [7]. This interest obviously boosted the research in medical imaging and digital diagnosis systems.

1.1 Feature Extraction

Feature vectors are used to represent a given image or give a specific information about a given image. In most of the image classification problems, feature vectors are used instead of pixel values of the image in the classification algorithms. Depending on the classification task, some features may require more emphasis and some may require less. If the aim is to detect red objects in a given image, it is expected that more features are extracted from the red channel of RGB color space and less features are extracted from other channels. Hence, more useful information about the image can be obtained for the specific classification task by choosing features properly.

In this thesis, the main challenge is that cancer stem cells (CSC) cannot be observed by naked eye in H&E stained liver tissues, although our task is to classify images according to their CSC ratios. Therefore, feature extraction gained prominence, since other distinguishing features in the images need to be exploited. This leads to an image classification based on their texture differences. We use discrete derivative of color histograms as features along with standard color histograms in Chapter 2. Additionally, pixel thresholding is applied to color histograms in order to avoid extracting features from empty or meaningless areas of a given image. When there are more than one feature vector, feature vectors can be concatenated to have one single feature vector or they can be cascaded to form a 2-D feature matrix. Covariance matrix of the feature matrix can also be used to obtain a more compact and smaller form of the feature matrix, which reduces the processing time and speeds up the classification process.

Scale invariant feature transform (SIFT), local binary patterns (LBP) and directional feature extraction algorithms are also used to obtain features from a given image in different directions in Chapter 3 [8]. The importance of choosing the right feature extraction method can clearly be seen by comparing the classification accuracies in Chapter 2 and Chapter 3.

1.2 Microscopic Image Classification

Image classification is the next step after feature extraction. In this thesis, we focus on diagnosis and grading of H&E stained liver tissue images. We propose a modified version of Principal Component Analysis (PCA) algorithm, which takes covariance matrices of feature matrices of images instead of pixel values of images as input for texture classification. This algorithm is similar to the well-known eigenface algorithm [9, 10], which compares images in the eigenspace.

In Chapter 2, color space features are fed into the modified PCA algorithm. In Chapter 3, directional feature set is used by modified PCA algorithm. In Chapter 4, distance calculation in modified PCA algorithm is replaced by multiplication-free operators to reduce the computational cost of the CAD system. In this case, color space features are used. In Chapter 5, obtained results are discussed and final remarks are made.

Chapter 2

CSC Image Classification with Modified Principal Component Analysis Algorithm

H&E stain is a cost effective histopathological technique [11–23]. It is hard to distinguish CSCs in H&E images, unlike CD13 stained images. CSCs can easily be distinguished in CD13 images, however it is an expensive stain. Therefore, a method that can classify H&E images considering their CSC densities would be more feasible and accessible. In this chapter, a classification method that classifies H&E images according to their CSC densities will be developed.

First, a brief explanation of the acquisition process of the histopathological images from the patients is given. In the acquisition process first, a sample tissue is taken from a patient and it is sliced in very thin layers. The successive layers look very similar, but they are not exactly the same. Since a stained layer cannot be stained again with another stain, it is not possible to have both CD13 and H&E stained versions of the same tissue layer. Therefore, successive layers are stained with CD13 and H&E stains assuming that they have almost the same visual properties (see Figure 2.1). Based on this assumption, CSC densities are calculated using CD13 stained layers to construct ground truth labels for

corresponding H&E images.

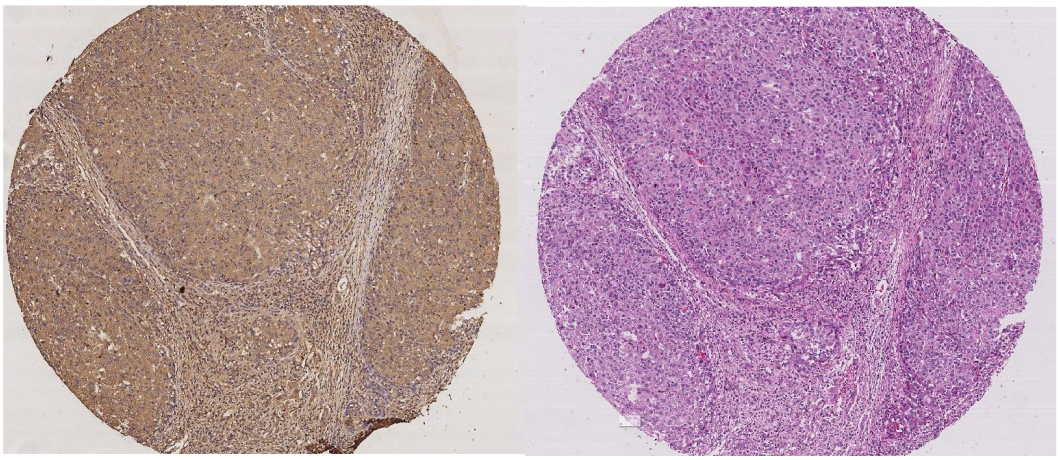

Figure 2.1: CD13 (left) and H&E (right) stained successive tissue layer images of the same patient.

In Figure 2.1, the successive layer images of the same tissue stained with CD13 and H&E are shown. CSC density in the chosen region is defined as the ratio of number of CSCs to number of all cells. This density is calculated on an arbitrarily chosen image region of CD13 stained tissue layer. The calculated density is assumed to be the same in the corresponding region of the successive H&E stained layer. The CSC density in the chosen region is calculated as follows:

$$CSC\ Ratio = \frac{\sum CSC}{\sum All\ Cells} \tag{2.1}$$

A grading scheme is defined according to CSC percentages. If the CSC Percentage is less than 5%, that region is labeled as Grade I. If it is greater than or equal to 5%, it is labeled as Grade II. If it is equal to 0%, it is labeled as normal, meaning that it contains no CSC. It is important to note that CD13 stained images are only used in labeling corresponding H&E tissue images. They are not involved in any part of the proposed method except extracting ground truth data.

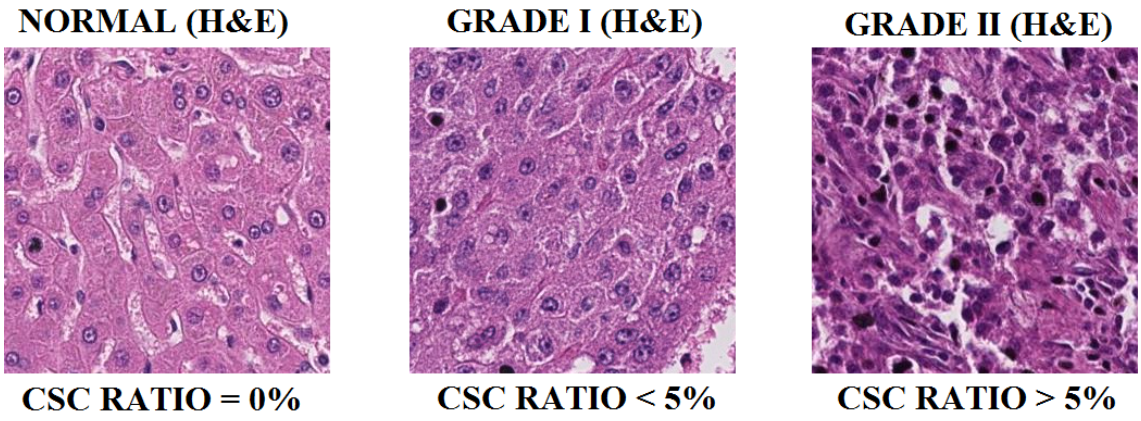

Figure 2.2: Sample H&E images according to calculated CSC levels.

In Figure 2.2, sample images of H&E stained normal, Grade I and Grade II tissue layers are shown. It is observed that the amount of darker regions increases as CSC ratio increases. This fact causes a significant pattern and color difference between three classes. Feature extraction methods are applied to these H&E images and obtained feature matrices are fed into the modified PCA algorithm for classification.

The proposed classification algorithm is similar to well-known eigenface algorithm [9]. Unlike conventional eigenface algorithm, covariance matrix of color histograms instead of pixel values are fed into the modified PCA algorithm. Histograms of the image, that of thresholded image, first and second order discrete derivative of them in various color spaces are used to construct the feature matrix. Our aim is to distinguish three classes of liver images; Grade I (Figure 2.4), Grade II (Figure 2.5), normal (Figure 2.3).

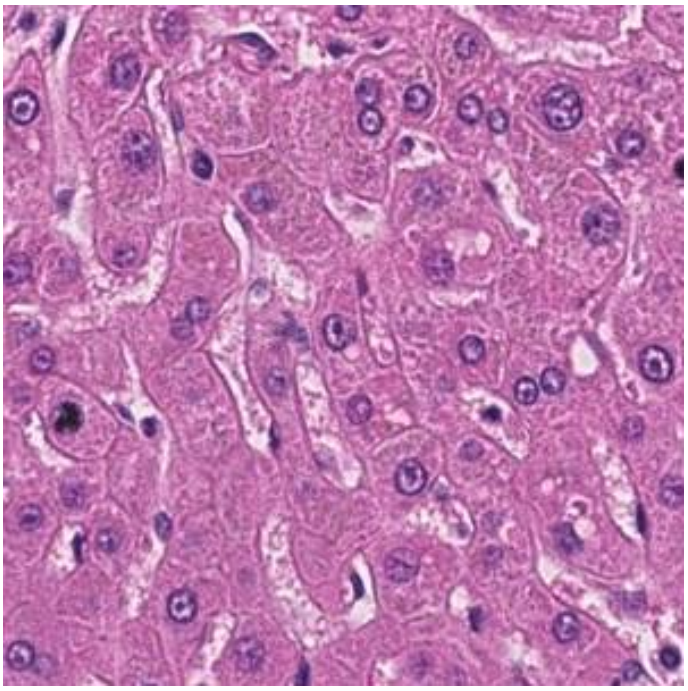

Figure 2.3: Microscopic Image of an H&E Stained Normal (CSC density= 0%) Liver Tissue Image

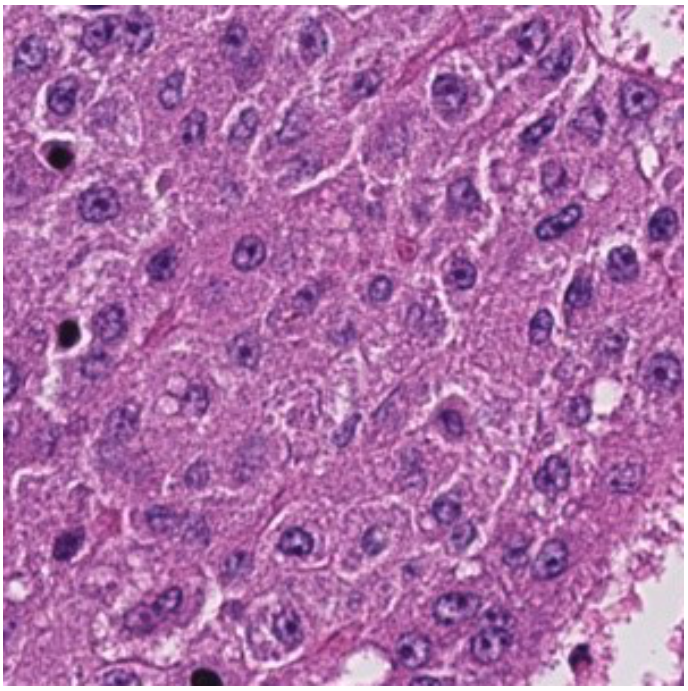

Figure 2.4: Microscopic Image of an H&E Stained Grade I (CSC density< 5%) Liver Tissue Image

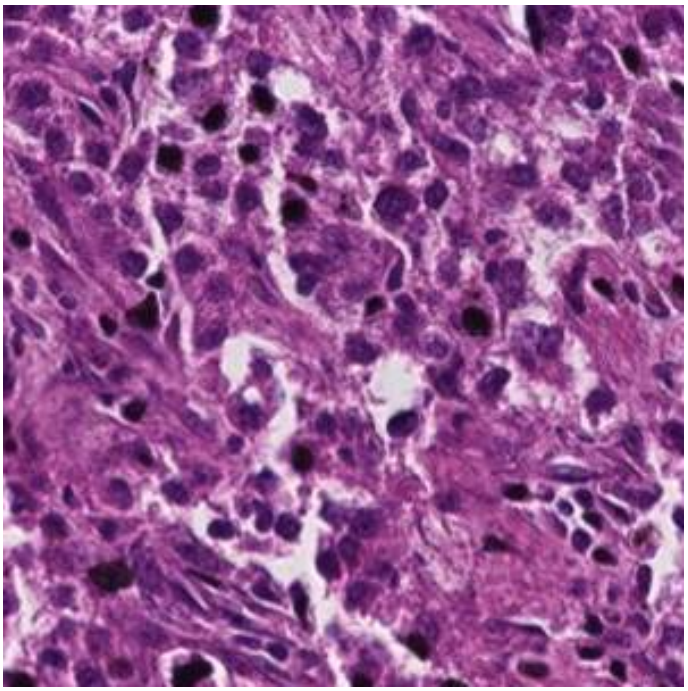

Figure 2.5: Microscopic Image of an H&E Stained Grade II (CSC density$>$ 5%) Liver Tissue Image

2.1 Modified PCA Algorithm

In this section, we propose a modified version of Principal Component Analysis (PCA) algorithm, which takes covariance matrices of feature matrices of images instead of pixel values of images as input for texture classification. In the proposed modified PCA algorithm, average covariance matrix of training set is calculated as follows:

$$C_V = \frac{1}{N} \sum_{i=1}^{N} F_i^T \times F_i \tag{2.2}$$

In Equation (2.2), N is the number of images in training set and F_i is the feature matrix of i^{th} image. Covariance matrix (C_V) of training set images is a 128x128 matrix. Eigenvalues λ_k and eigenvectors $\boldsymbol{u_k}$ of C_V are computed. The steps below are followed for comparing two images:

(i) Let $\boldsymbol{\gamma}$ be the average of columns of $F_m^T \times F_m$ and $\boldsymbol{\zeta}$ be average of columns of $F_n^T \times F_n$, where m is index of the reference image and n is index of the compared image.

(ii) The reference image is projected onto the 'cell space' by multiplying $\boldsymbol{\gamma}$ by the first 20 vectors of $\boldsymbol{u_k}$ (20 eigenvectors corresponding to 20 largest eigenvalues), as in Equation (2.3) where $\mu_{\boldsymbol{\gamma}}$ is the mean of $\boldsymbol{\gamma}$. In Figure 2.6, it is shown that largest 20 eigenvalues of the training set is significantly larger than the remaining eigenvalues.

$$v_k = \boldsymbol{u_k}^T(\boldsymbol{\gamma} - \mu_{\boldsymbol{\gamma}}), k = 1, 2, ..., 20 \tag{2.3}$$

Similarly, the compared image is projected onto the 'cell space' by multiplying $\boldsymbol{\zeta}$ by the first 20 vectors of $\boldsymbol{u_k}$ (20 eigenvectors corresponding to 20 largest eigenvalues), as in Equation (2.4) where $\mu_{\boldsymbol{\zeta}}$ is the mean of $\boldsymbol{\zeta}$.

$$w_k = \boldsymbol{u_k}^T(\boldsymbol{\zeta} - \mu_{\boldsymbol{\zeta}}), k = 1, 2, ..., 20 \tag{2.4}$$

(iii) The similarity between two images is defined as follows:

$$sim(I_1, I_2) = cos(\boldsymbol{v}, \boldsymbol{w}) = \frac{< \boldsymbol{v} \cdot \boldsymbol{w} >}{\|\boldsymbol{v}\|_2 \|\boldsymbol{w}\|_2} \tag{2.5}$$

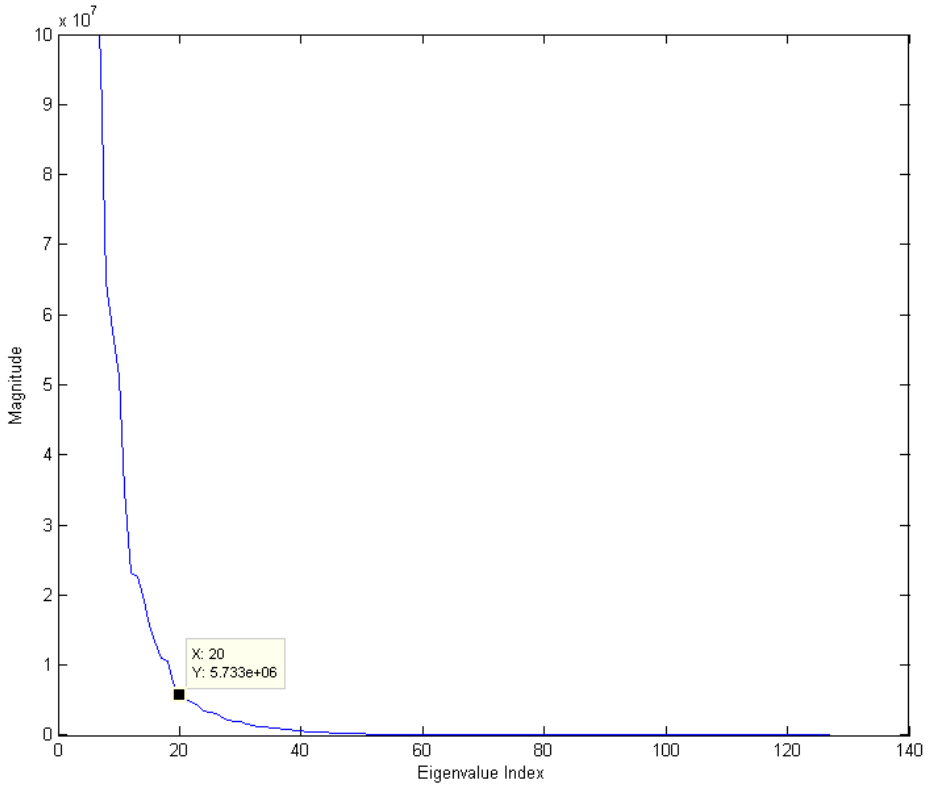

Figure 2.6: Eigenvalues of the Training Set When Query Image is Taken From the First Patient of Grade I Image Set

2.2 Feature Extraction from Color Spaces

The difference of three classes is their CSC ratio. Due to their higher CSC ratio, Grade II images have a tendency to have more dark regions than Grade I and normal images. Therefore, the proposed feature matrix utilizes color space histograms. All images in our dataset are acquired in RGB color space and converted to YUV, HE [17] and HSV color spaces for feature extraction. The

feature matrix is as follows:

$$\begin{aligned} F = [&hist(R) \quad hist(R_t) \quad hist(G) \quad hist(G_t) \quad hist(B) \quad hist(B_t) \quad hist(Y) \\ &hist(Y)' \quad hist(Y_t) \quad hist(U) \quad hist(U)' \quad hist(U)'' \quad hist(V) \quad hist(V)' \\ &hist(V)'' \quad hist(H) \quad hist(H_t) \quad hist(E) \quad hist(S) \quad hist(S_t)]^T \end{aligned} \tag{2.6}$$

,where R is red channel, G is green channel, B is blue channel of RGB color space

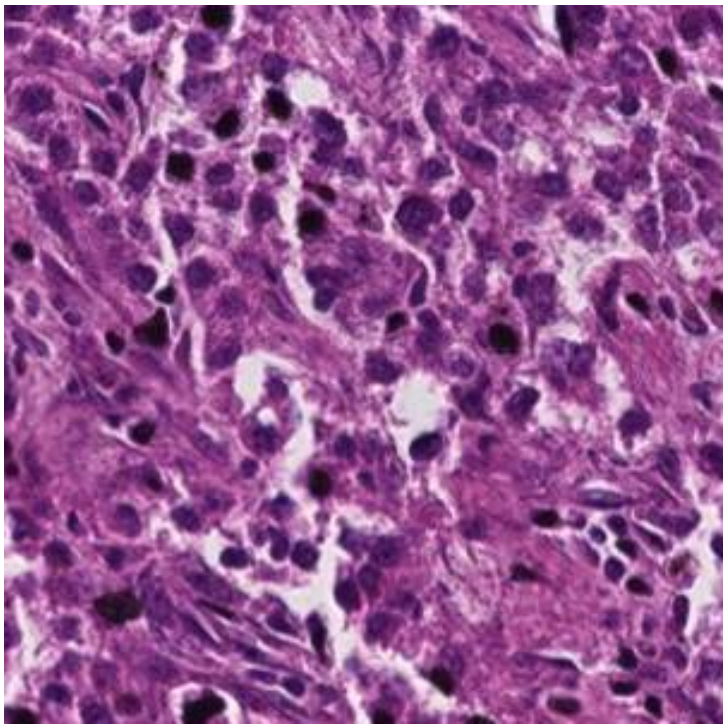

Figure 2.7: 3-Channel (RGB) Liver Image

respectively; Y is luminance channel, U and V are chrominance channels of YUV color space respectively; H is Hematoxylin channel, E is Eosin channel of HE color space respectively and S is saturation channel of HSV colorspace. The $hist(\cdot)$ function computes a 128-bin histogram of a given input. The $hist(\cdot)'$ function denotes the first order discrete derivative of $hist(\cdot)$, $hist(\cdot)''$ function denotes the second order discrete derivative of $hist(\cdot)$ and $(\cdot_t)$ denotes pixel thresholding in that specified channel. Pixel thresholding is utilized to extract more descriptive features from darker regions[1]. In the experiments, this threshold is empirically

[1]Adjectives dark and bright are defined according to RGB color space.

selected as 200. In R, G, B, Y, U, V and E channels, pixel values greater than 200 are discarded. However, in H and S channels, pixel values smaller than 200 are discarded. Therefore, more representative features of 'darker regions' are extracted. In Equation 2.6, $hist(\cdot)$ function produces a column vector of size 128×1 in the range [0,255]. A feature matrix F of size 20x128 for each image is obtained by cascading each histogram output..

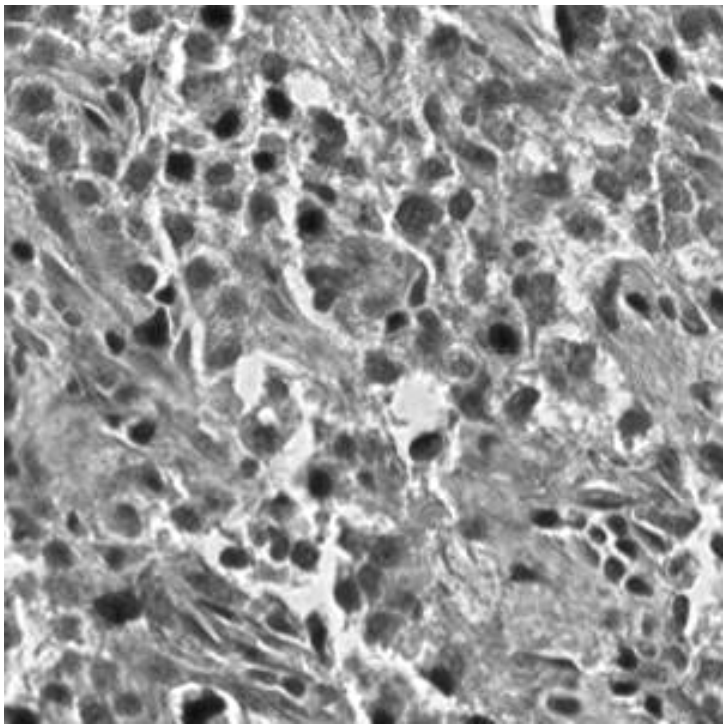

Figure 2.8: R Channel of an H&E Stained RGB Liver Tissue Image

2.3 Experimental Results

Our dataset consists of three classes of H&E stained liver images; Grade I (119 images taken from 17 patients), Grade II (151 images taken from 17 patients) and normal (184 images taken from 9 patients) tissue images. three-nearest neighbor classification is used to determine the class of a test image. Instead of leave-one-image-out strategy, leave-one-patient-out strategy is used; since each patient has more than one image. The term 'patient classification accuracy' is defined in order

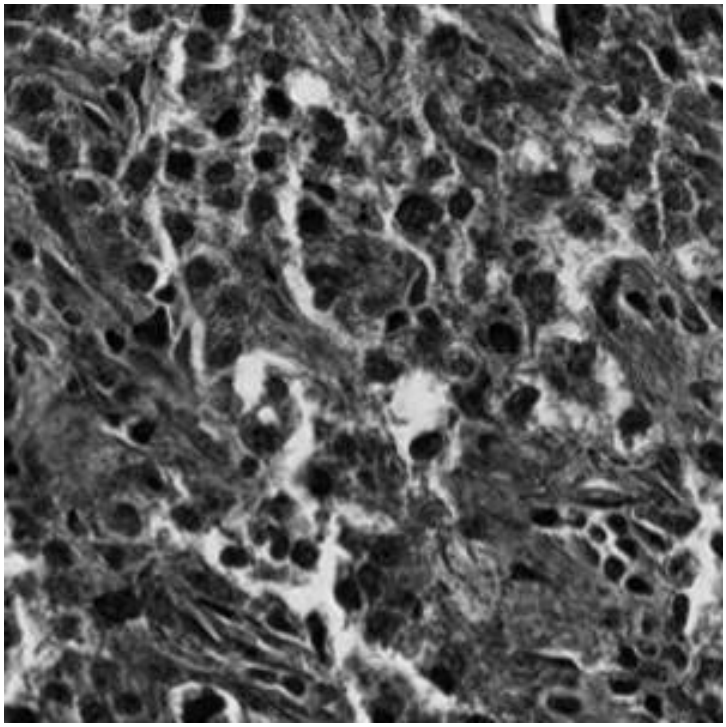

Figure 2.9: G Channel of an H&E Stained RGB Liver Tissue Image

to make a decision about patients. In order to classify a patient, majority voting is employed among the decisions of the patient's images. The test set is circulated to cover all instances and contains one image at each iteration. Throughout this thesis, recall (2.7), precision (2.8) and overall accuracy (2.9) are used to measure the performance of designed CAD systems.

$$Recall = \frac{\sum TruePositives}{\sum TruePositives + \sum FalseNegatives} \tag{2.7}$$

$$Precision = \frac{\sum TruePositives}{\sum TruePositives + \sum FalsePositives} \tag{2.8}$$

$$OverallAccuracy = \frac{\sum TruePositives + \sum TrueNegatives}{\sum TotalPopulation} \tag{2.9}$$

As seen in Tables 2.1 and 2.2, 74.7% and 74.4% classification accuracies are

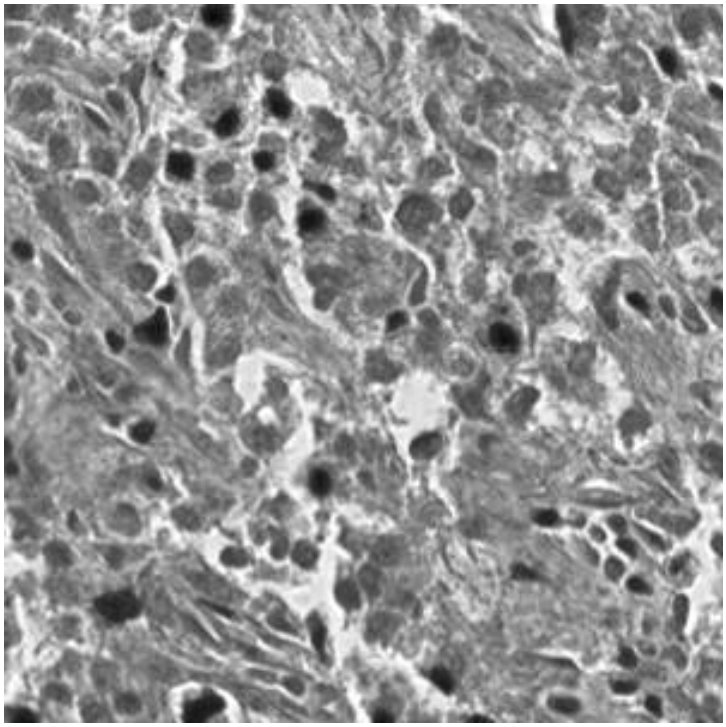

Figure 2.10: B Channel of an H&E Stained RGB Liver Tissue Image

achieved in three-class image and patient classification respectively. It is important to emphasize that normal image classification accuracy is 89.8%. It is also observed that image and patient classification accuracies of the same cases may differ significantly due to the majority voting applied in the patient classification.

In Tables 2.3 and 2.4, Grade I and Grade II images together constitute the cancerous class. In this case, overall image classification is 93.0%. Another important point is that cancerous image classification accuracy is 93.3% and normal image classification accuracy is 90.2%.

In Tables 2.5 and 2.6, normal images are excluded from the dataset and classification is performed among cancerous images. In this case, image classification accuracy is 70.4% and patient classification accuracy is 73.5%.

It is experimentally observed that modified PCA algotihm with color space features achieves significant accuracies in two-class and three-class classification and grading problem.

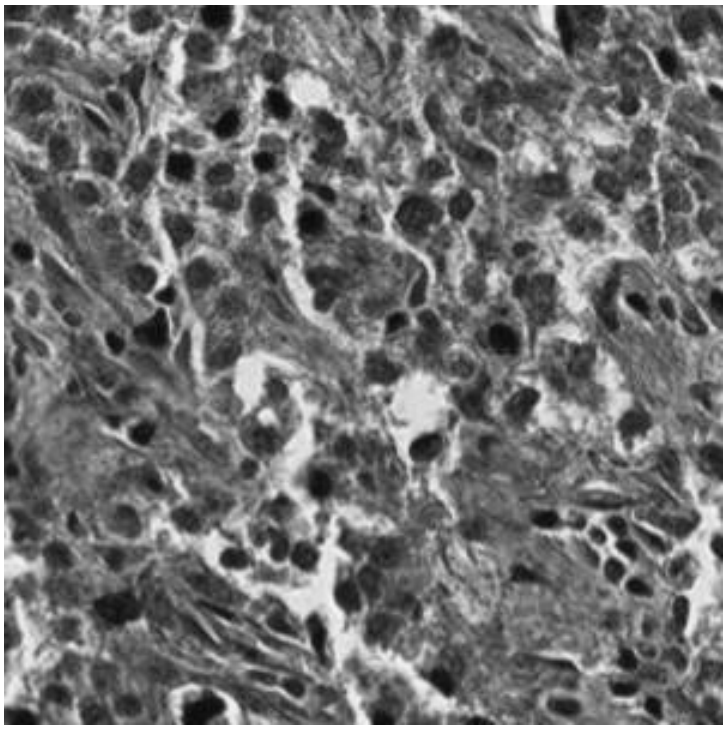

Figure 2.11: Y Channel of an H&E Stained YUV Liver Tissue Image

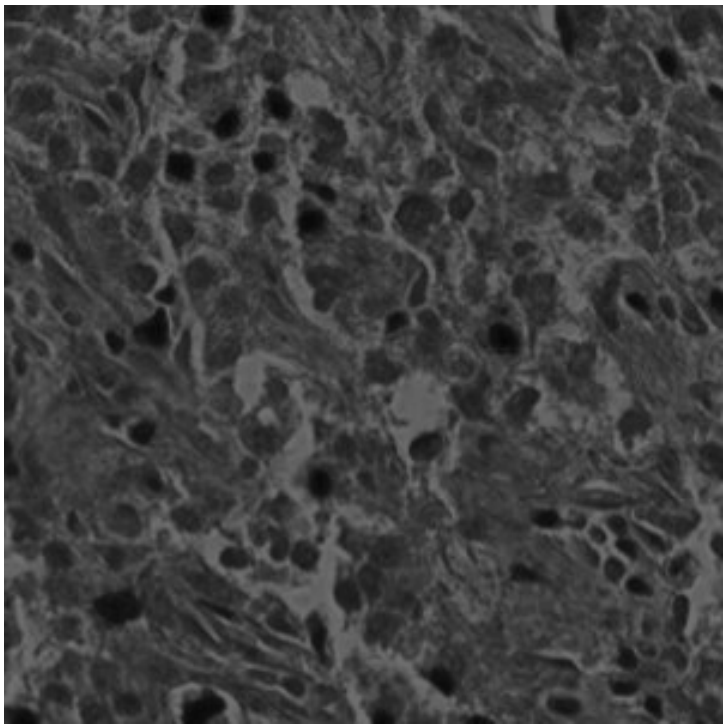

Figure 2.12: U Channel of an H&E Stained YUV Liver Tissue Image

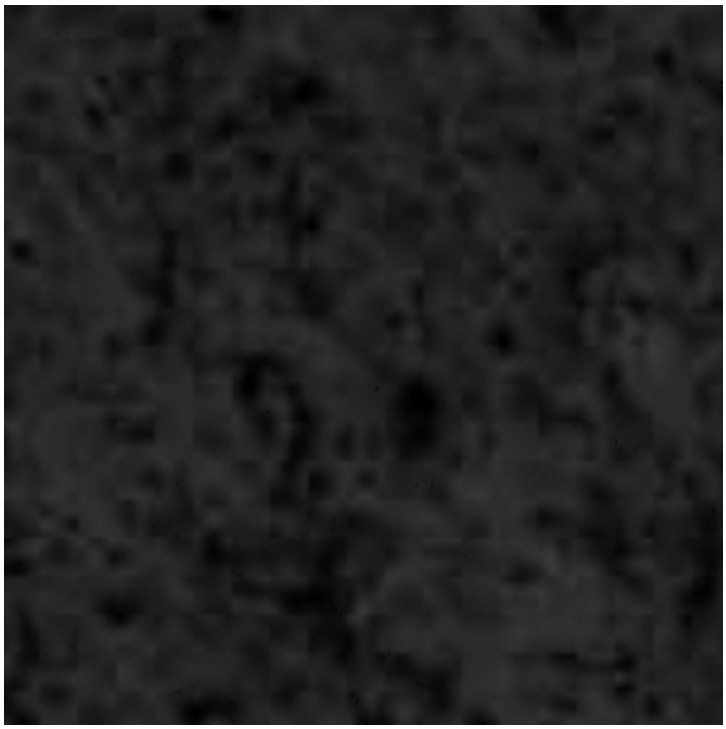

Figure 2.13: V Channel of an H&E Stained YUV Liver Tissue Image

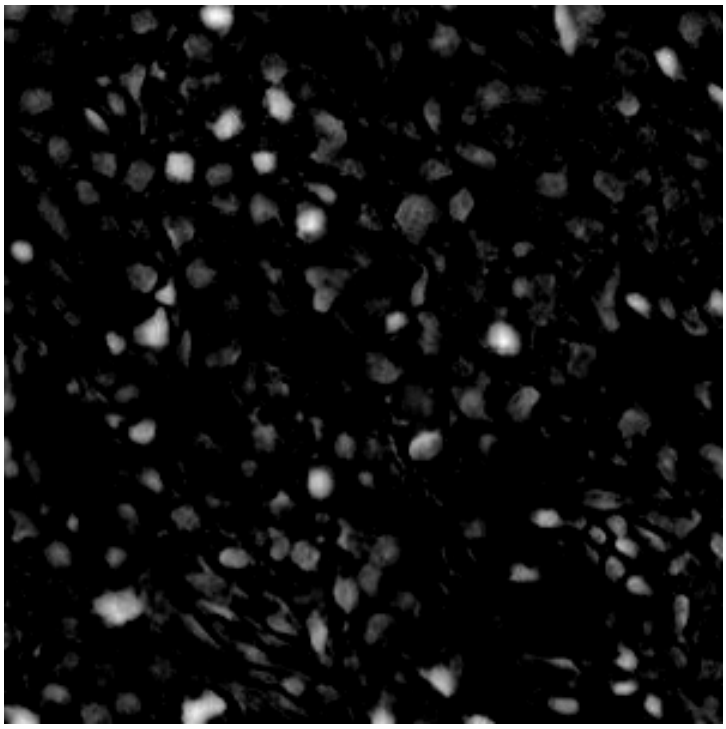

Figure 2.14: H Channel of an H&E Stained HE Liver Tissue Image

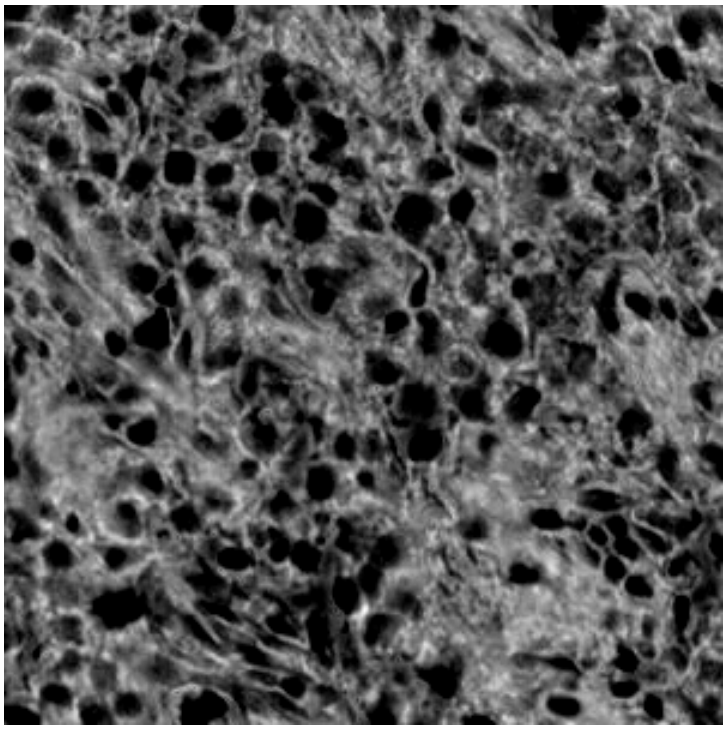

Figure 2.15: E Channel of an H&E Stained HE Liver Tissue Image

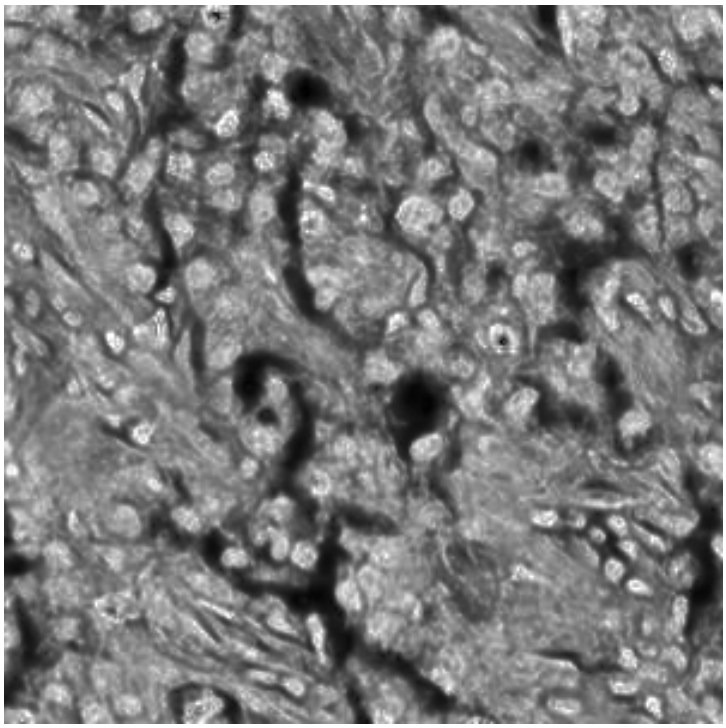

Figure 2.16: S Channel of an H&E Stained HSV Liver Tissue Image

Table 2.1: Confusion Matrix of Three-Class 3-NN Modified PCA Image Classification Using Color Space Features

	Grade I	Grade II	Normal	Recall
Grade I	70/119	41/119	8/119	58.8%
Grade II	38/151	102/151	11/151	67.5%
Normal	12/184	5/184	167/184	90.8%
Precision	58.3%	68.9%	89.8%	Overall Accuracy 74.7%

Table 2.2: Confusion Matrix of Three-Class 3-NN Modified PCA Patient Classification Using Color Space Features

	Grade I	Grade II	Normal	Recall
Grade I	11/17	5/17	1/17	64.7%
Grade II	3/17	12/17	2/17	70.6%
Normal	0/9	0/9	9/9	100%
Precision	78.6%	70.6%	75.0%	Overall Accuracy 74.4%

Table 2.3: Confusion Matrix of Two-Class (Healthy vs. Cancerous) 3-NN Modified PCA Image Classification Using Color Space Features

	Cancerous	Normal	Recall
Cancerous	252/270	18/270	93.3%
Normal	18/184	166/184	90.2%
Precision	93.3%	90.2%	Overall Accuracy 92.1%

Table 2.4: Confusion Matrix of Two-Class (Healthy vs. Cancerous) 3-NN Modified PCA Patient Classification Using Color Space Features

	Cancerous	Normal	Recall
Cancerous	31/34	3/34	91.2%
Normal	0/0	9/9	100%
Precision	100%	75.0%	Overall Accuracy 93.0%

Table 2.5: Confusion Matrix of Two-Class (Grade I vs. Grade II) 3-NN Modified PCA Image Classification Using Color Space Features

	Grade I	Grade II	Recall
Grade I	77/119	42/119	64.7%
Grade II	38/151	113/151	74.8%
Precision	67.0%	72.9%	Overall Accuracy 70.4%

Table 2.6: Confusion Matrix of Two-Class (Grade I vs. Grade II) 3-NN Modified PCA Patient Classification Using Color Space Features

	Grade I	Grade II	Recall
Grade I	11/17	6/17	64.7%
Grade II	3/17	14/17	82.4%
Precision	78.6%	70.0%	Overall Accuracy 73.5%

2.4 Comparison With SIFT Features

Scale Invariant Feature Transform (SIFT) is a widely used feature extraction method for object recognition problems [24–26]. This algorithm aims to extract scale and rotation invariant features of images. Previous studies show that this algorithm performs robust object recognition. In this section, we will extract SIFT features from our histopathological image dataset and compare them with color space histogram features on our three-class texture classification problem.

In this thesis, Lowe's SIFT implementation and source codes are used [27]. This implementation is composed of four steps; scale-space extrema detection, keypoint localization, orientation assignment and keypoint descriptor. In the first step, difference-of-Gaussian function is used to identify potential points that are invariant to scale and orientation. At keypoint localization stage, keypoints are selected among all candidate points based on measures of their stability. Then, one or more orientations are assigned to each keypoint location based on local image gradient directions for orientation assignment. In the last step, histogram of image gradients is computed for eight orientation bins and stored in the feature vector, which is the vector representation of the keypoint descriptor. The feature vector contains magnitudes of the elements of histogram of image gradients. A sample image gradients and keypoint descriptor are shown in Figure 2.17 [2].

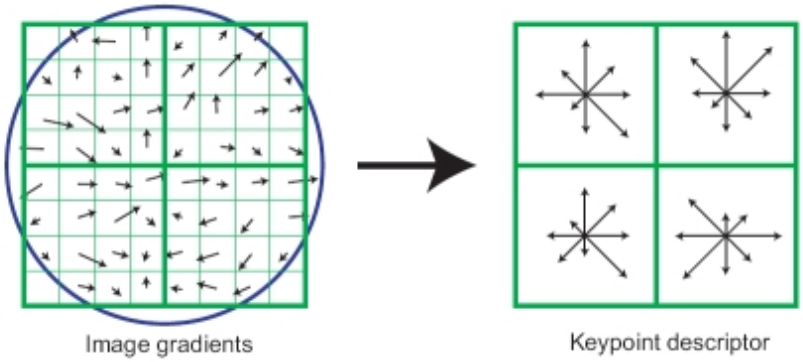

Figure 2.17: Obtaining Keypoint Descriptor from Image Gradients for Eight Orientation Bins

[2]This figure is taken from [25].

In the experiments, histograms of gradients are taken from a 4×4 descriptor window computed from a 16×16 sample array around the keypoint. Since, histograms of image gradients are computed in eight orientation bins, resulting feature vector is 128-element. A CSC image has N keypoints, so a feature matrix is of size $N \times 128$ is obtained by cascading all feature vectors of keypoints. This feature matrix is fed into the modified PCA algorithm and 3-NN classification is performed.

In Figure 2.18, keypoints found by Lowe's SIFT algorithm on Y channel of an H&E stained liver tissue image is shown. Keypoints are mostly found on darker regions as desired.

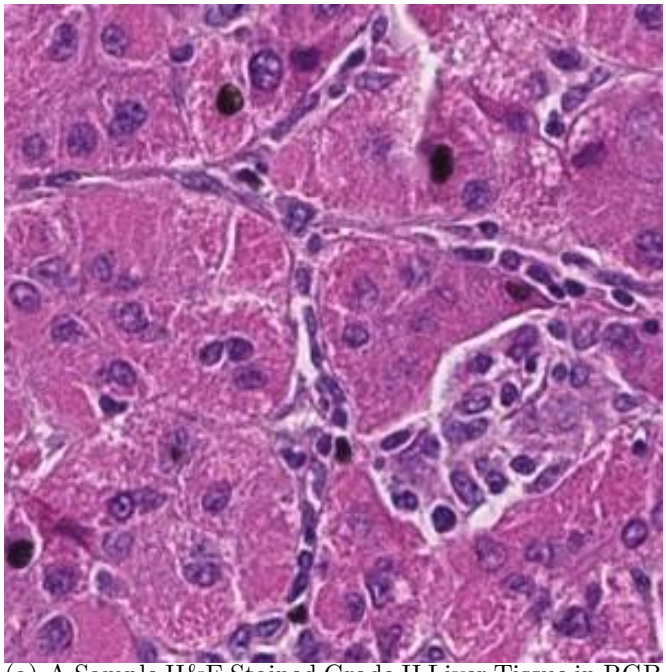

(a) A Sample H&E Stained Grade II Liver Tissue in RGB Color Space

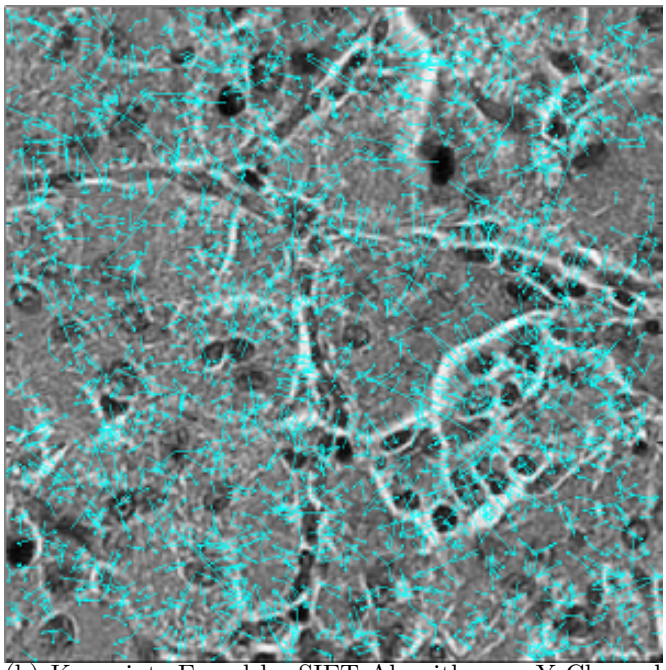

(b) Keypoints Found by SIFT Algorithm on Y Channel of an H&E Stained Grade II Liver Tissue Image

Figure 2.18: Keypoints Found by SIFT Algorithm on Y Channel of an H&E Stained Grade II Liver Tissue Image

2.4.1 Experimental Results with Single-Channel Features

The same dataset in Section 2.3 is used which has 454 images of three classes. First, SIFT features are extracted from Y channels of input images, because SIFT algorithm extract features from single-channel image data. Classification and grading performance of the modified PCA algorithm using SIFT features will be observed and compared with the results obtained by color space features.

Table 2.7: Confusion Matrix of Three-Class 3-NN Modified PCA Image Classification Using SIFT Features of Y Channel

	Grade I	Grade II	Normal	Recall
Grade I	34/119	65/119	20/119	28.6%
Grade II	60/151	45/151	46/151	29.8%
Normal	11/184	37/184	136/184	73.9%
Precision	32.4%	30.6%	67.3%	Overall Accuracy 47.4%

Table 2.8: Confusion Matrix of Three-Class 3-NN Modified PCA Patient Classification Using SIFT Features of Y Channel

	Grade I	Grade II	Normal	Recall
Grade I	4/17	11/17	2/17	23.5%
Grade II	9/17	3/17	5/17	17.6%
Normal	0/9	0/9	9/9	100%
Precision	30.8%	21.4%	56.3%	Overall Accuracy 37.2%

As seen in Tables 2.7 and 2.8, 47.4% image classification accuracy and 37.2% patient classification accuracy is obtained by SIFT features. These accuracies are far smaller than the accuracies obtained by color space features (Tables 2.1 and 2.2). In this case, the best recognition performance is observed in normal class images.

In Tables 2.9 and 2.10, image classification accuracy is 75.5% and patient classification accuracy is 81.4%. In this case, it is shown that significant classification

Table 2.9: Confusion Matrix of Two-Class (Healthy vs. Cancerous) 3-NN Modified PCA Image Classification Using SIFT Features of Y Channel

	Cancerous	Normal	Recall
Cancerous	208/270	62/270	77.0%
Normal	49/184	135/184	73.4%
Precision	80.9%	68.5%	Overall Accuracy 75.5%

Table 2.10: Confusion Matrix of Two-Class (Healthy vs. Cancerous) 3-NN Modified PCA Patient Classification Using SIFT Features of Y Channel

	Cancerous	Normal	Recall
Cancerous	27/34	7/34	79.4%
Normal	1/9	8/9	88.9%
Precision	96.4%	53.3%	Overall Accuracy 81.4%

accuracies can be obtained by SIFT features, but these results are not comparable to the results obtained by color space features (Tables 2.3 and 2.4).

Table 2.11: Confusion Matrix of Two-Class (Grade I vs. Grade II) 3-NN Modified PCA Image Classification Using SIFT Features of Y Channel

	Grade I	Grade II	Recall
Grade I	50/119	69/119	42.0%
Grade II	67/151	84/151	55.6%
Precision	42.7%	54.9%	Overall Accuracy 49.6%

In Tables 2.11 and 2.12, cancerous tissues are graded in two-class case. Image classification accuracy is 49.6% and patient classification accuracy is 41.2%. These results are not comparable to the results obtained by color space features (Tables 2.11 and 2.12).

Considering all three cases of classification and grading of H&E stained liver tissue images, it is experimentally observed that SIFT features can distinguish

Table 2.12: Confusion Matrix of Two-Class (Grade I vs. Grade II) 3-NN Modified PCA Patient Classification Using SIFT Features of Y Channel

	Grade I	Grade II	Recall
Grade I	6/17	11/17	35.3%
Grade II	9/17	8/17	47.1%
Precision	60.0%	42.1%	Overall Accuracy 41.2%

cancerous and normal tissues (two-class healthy vs. cancerous case). However, they do not produce good results in two-class grading of cancerous tissue images and three-class classification case.

2.4.2 Experimental Results with Multi-Channel Features

The same dataset in Section 2.3 is used which has 454 images of three classes. In this subsection, SIFT features are extracted from various color channels separately and then extracted SIFT feature matrices are cascaded horizontally to form the feature matrix. In the experiments we analyze three multi-channel cases using combinations of Y channel of YUV color space, H channel and E channel of HE color space and R channel, G channel and B channel of RGB color space. Classification and grading performance of the modified PCA algorithm using multi-channel SIFT features will be observed and compared with the results obtained by single-channel SIFT features and histograms of color space features.

First, features are extracted from Y, H and E channels and obtained results are compared with the results obtained in single-channel case.

As seen in Tables 2.13 and 2.14, 53.7% image classification accuracy and 44.2% patient classification accuracy is obtained by multi-channel SIFT features extracted from Y, H and E channels. These accuracies are better than the accuracies obtained by single-channel SIFT features extracted from Y channel (Tables 2.7 and 2.8). In three-class case, using multi-channel SIFT features improves the

Table 2.13: Confusion Matrix of Three-Class 3-NN Modified PCA Image Classification Using SIFT Features of Y, H and E Channels

	Grade I	Grade II	Normal	Recall
Grade I	38/119	64/119	17/119	31.9%
Grade II	64/151	60/151	27/151	39.7%
Normal	9/184	29/184	146/184	79.3%
Precision	34.2%	39.2%	76.8%	Overall Accuracy 53.7%

Table 2.14: Confusion Matrix of Three-Class 3-NN Modified PCA Patient Classification Using SIFT Features of Y, H and E Channels

	Grade I	Grade II	Normal	Recall
Grade I	4/17	10/17	3/17	23.5%
Grade II	9/17	6/17	2/17	35.3%
Normal	0/9	0/9	9/9	100%
Precision	30.8%	62.5%	64.3%	Overall Accuracy 44.2%

classification performance of the system.

Table 2.15: Confusion Matrix of Two-Class (Healthy vs. Cancerous) 3-NN Modified PCA Image Classification Using SIFT Features of Y, H and E Channels

	Cancerous	Normal	Recall
Cancerous	208/270	62/270	77.0%
Normal	49/184	135/184	73.4%
Precision	80.9%	68.5%	Overall Accuracy 75.5%

In Tables 2.15 and 2.16, image classification accuracy is 75.5% and patient classification accuracy is 81.4%. In this case, obtained results are the same as the results obtained by single-channel SIFT features (Tables 2.9 and 2.10).

In Tables 2.17 and 2.18, image classification accuracy is 49.6% and patient classification accuracy is 41.2%. In this case, obtained results are the same as the

Table 2.16: Confusion Matrix of Two-Class (Healthy vs. Cancerous) 3-NN Modified PCA Patient Classification Using SIFT Features of Y, H and E Channels

	Cancerous	Normal	Recall
Cancerous	27/34	7/34	79.4%
Normal	1/9	8/9	88.9%
Precision	96.4%	53.3%	Overall Accuracy 81.4%

Table 2.17: Confusion Matrix of Two-Class (Grade I vs. Grade II) 3-NN Modified PCA Image Classification Using SIFT Features of Y, H and E Channels

	Grade I	Grade II	Recall
Grade I	50/119	69/119	42.0%
Grade II	67/151	84/151	55.6%
Precision	42.7%	54.9%	Overall Accuracy 49.6%

results obtained by single-channel SIFT features (Tables 2.11 and 2.12).

In multi-channel case of SIFT that uses Y, H and E channels for feature extraction, it is observed that it outperforms single-channel case in three-class classification and it produces same results as the single-channel case in two-class classifications. Therefore, six color channels are used in the next multi-channel case.

In the second multi-channel case of SIFT, features are extracted from Y, H, E, R, G and B channels and obtained results are compared with the results obtained in single-channel case and previous multi-channel case.

As seen in Tables 2.19 and 2.20, 53.7% image classification accuracy and 44.2% patient classification accuracy is obtained by multi-channel SIFT features extracted from Y, H, E, R, G and B channels. These classification accuracies are better than the accuracies obtained by single-channel SIFT features extracted from Y channel (Tables 2.7 and 2.8) and the same as the previous multi-channel case.

Table 2.18: Confusion Matrix of Two-Class (Grade I vs. Grade II) 3-NN Modified PCA Patient Classification Using SIFT Features of Y, H and E Channels

	Grade I	Grade II	Recall
Grade I	6/17	11/17	35.3%
Grade II	9/17	8/17	47.1%
Precision	60.0%	42.1%	Overall Accuracy 41.2%

Table 2.19: Confusion Matrix of Three-Class 3-NN Modified PCA Image Classification Using SIFT Features of Y, H, E, R, G and B Channels

	Grade I	Grade II	Normal	Recall
Grade I	38/119	64/119	17/119	31.9%
Grade II	64/151	60/151	27/151	39.7%
Normal	9/184	29/184	146/184	79.3%
Precision	34.2%	39.2%	76.8%	Overall Accuracy 53.7%

In Tables 2.21 and 2.22, image classification accuracy is 75.5% and patient classification accuracy is 81.4%. These classification accuracies are better than the accuracies obtained by single-channel SIFT features extracted from Y channel (Tables 2.9 and 2.10) and the same as the previous multi-channel case.

In Tables 2.23 and 2.24, image classification accuracy is 49.6% and patient classification accuracy is 41.2%. These classification accuracies are better than the accuracies obtained by single-channel SIFT features extracted from Y channel (Tables 2.11 and 2.12) and the same as the previous multi-channel case.

In multi-channel implementation of SIFT that extracts features from six color channels (Y, H, E, R, G, B), it is observed that it produces better results than the single-channel case. However, it produces the same results as the previous multi-channel case that utilizes three channels (Y, H, E). Therefore, in the next multi-channel case, three color channels are used.

In the third multi-channel case of SIFT, features are extracted from R, G

Table 2.20: Confusion Matrix of Three-Class 3-NN Modified PCA Patient Classification Using SIFT Features of Y, H, E, R, G and B Channels

	Grade I	Grade II	Normal	Recall
Grade I	4/17	10/17	3/17	23.5%
Grade II	9/17	6/17	2/17	35.3%
Normal	0/9	0/9	9/9	100%
Precision	30.8%	62.5%	64.3%	Overall Accuracy 44.2%

Table 2.21: Confusion Matrix of Two-Class (Healthy vs. Cancerous) 3-NN Modified PCA Image Classification Using SIFT Features of Y, H, E, R, G and B Channels

	Cancerous	Normal	Recall
Cancerous	208/270	62/270	77.0%
Normal	49/184	135/184	73.4%
Precision	80.9%	68.5%	Overall Accuracy 75.5%

and B channels and obtained results are compared with the results obtained in single-channel case and previous multi-channel cases.

As seen in Tables 2.25 and 2.26, 56.4% image classification accuracy and 48.8% patient classification accuracy is obtained by multi-channel SIFT features extracted from R, G and B channels. These classification accuracies are better than the accuracies obtained in all previous SIFT based three-class cases. However, they are not better than the accuracies obtained by color space features (Tables 2.1 and 2.2).

In Tables 2.27 and 2.28, image classification accuracy is 78.9% and patient classification accuracy is 86.1%. These classification accuracies are better than the accuracies obtained in all previous SIFT based 'cancerous or not' cases. However, they are not better than the accuracies obtained by color space features (Tables 2.3 and 2.4).

Table 2.22: Confusion Matrix of Two-Class (Healthy vs. Cancerous) 3-NN Modified PCA Patient Classification Using SIFT Features of Y, H, E, R, G and B Channels

	Cancerous	Normal	Recall
Cancerous	27/34	7/34	79.4%
Normal	1/9	8/9	88.9%
Precision	96.4%	53.3%	Overall Accuracy 81.4%

Table 2.23: Confusion Matrix of Two-Class (Grade I vs. Grade II) 3-NN Modified PCA Image Classification Using SIFT Features of Y, H, E, R, G and B Channels

	Grade I	Grade II	Recall
Grade I	50/119	69/119	42.0%
Grade II	67/151	84/151	55.6%
Precision	42.7%	54.9%	Overall Accuracy 49.6%

In Tables 2.29 and 2.30, image classification accuracy is 49.6% and patient classification accuracy is 41.2%. These classification accuracies are better than the accuracies obtained by single-channel SIFT features extracted from Y channel (Tables 2.11 and 2.12) and the same as the previous multi-channel two-class grading cases.

Briefly, the best classification accuracies are obtained with multi-channel SIFT features that are extracted from R, G and B channels. However, these classification accuracies are not better than the accuracies obtained by color space features.

Table 2.24: Confusion Matrix of Two-Class (Grade I vs. Grade II) 3-NN Modified PCA Patient Classification Using SIFT Features of Y, H, E, R, G and B Channels

	Grade I	Grade II	Recall
Grade I	6/17	11/17	35.3%
Grade II	9/17	8/17	47.1%
Precision	60.0%	42.1%	Overall Accuracy 41.2%

Table 2.25: Confusion Matrix of Three-Class 3-NN Modified PCA Image Classification Using SIFT Features of R, G and B Channels

	Grade I	Grade II	Normal	Recall
Grade I	40/119	63/119	16/119	33.6%
Grade II	58/151	70/151	23/151	46.4%
Normal	11/184	27/184	146/184	79.3%
Precision	36.7%	43.8%	78.9%	Overall Accuracy 56.4%

Table 2.26: Confusion Matrix of Three-Class 3-NN Modified PCA Patient Classification Using SIFT Features of R, G and B Channels

	Grade I	Grade II	Normal	Recall
Grade I	5/17	10/17	2/17	29.4%
Grade II	8/17	7/17	2/17	41.2%
Normal	0/9	0/9	9/9	100%
Precision	38.5%	41.2%	69.2%	Overall Accuracy 48.8%

Table 2.27: Confusion Matrix of Two-Class (Healthy vs. Cancerous) 3-NN Modified PCA Image Classification Using SIFT Features of R, G and B Channels

	Cancerous	Normal	Recall
Cancerous	219/270	51/270	81.1%
Normal	45/184	139/184	75.5%
Precision	83.0%	73.2%	Overall Accuracy 78.9%

Table 2.28: Confusion Matrix of Two-Class (Healthy vs. Cancerous) 3-NN Modified PCA Patient Classification Using SIFT Features of R, G and B Channels

	Cancerous	Normal	Recall
Cancerous	29/34	5/34	85.3%
Normal	1/9	8/9	88.9%
Precision	96.7%	61.5%	Overall Accuracy 86.1%

Table 2.29: Confusion Matrix of Two-Class (Grade I vs. Grade II) 3-NN Modified PCA Image Classification Using SIFT Features of R, G and B Channels

	Grade I	Grade II	Recall
Grade I	51/119	68/119	42.9%
Grade II	68/151	83/151	55.0%
Precision	42.9%	55.0%	Overall Accuracy 49.6%

Table 2.30: Confusion Matrix of Two-Class (Grade I vs. Grade II) 3-NN Modified PCA Patient Classification Using SIFT Features of R, G and B Channels

	Grade I	Grade II	Recall
Grade I	6/17	11/17	35.3%
Grade II	9/17	8/17	47.1%
Precision	60.0%	42.1%	Overall Accuracy 41.2%

2.5 Comparison With LBP Features

Local Binary Patterns (LBP) is another widely used feature extraction method for texture classification problems [28–32]. This algorithm is known to extract both texture and shape information of a given image. Ahonen's circular $(8, 2)$ neighborhood LBP model is used in this thesis and it is shown in Figure 2.19.

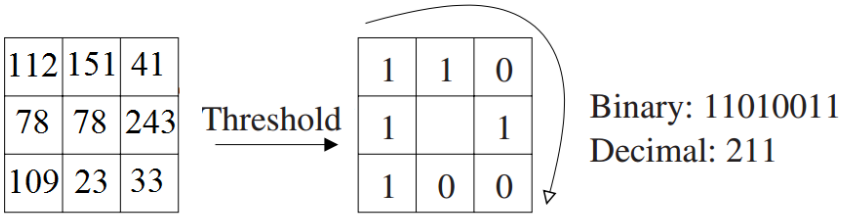

Figure 2.19: Circular $(8, 2)$ Neighborhood LBP Feature Extraction for one Pixel

In this LBP model, an 8-bit binary number is extracted from each pixel. Each pixel is visited and compared with its eight neighbors. Starting form top-left neighbor, if center pixel is greater than or equal to its neighbor '1' is written, otherwise '0' is written to construct the 8-bit feature number. This 8-bit binary number is converted to decimal and stored in the pattern vector. This process is repeated for each pixel in the image. Finally, 128-bin histogram of this pattern vector is computed to form the feature vector. In experiments, we only extracted LBP features from keypoints found by SIFT algorithm in order to reduce computational cost and extract features around cell parts. Eleven LBP feature vectors are extracted from eleven different color spaces as in Equation (2.10).

$$F_{LBP} = \begin{bmatrix} LBP_R \\ LBP_G \\ LBP_B \\ LBP_Y \\ LBP_U \\ LBP_V \\ LBP_H \\ LBP_E \\ LBP_{HH} \\ LBP_S \\ LBP_{VV} \end{bmatrix} \tag{2.10}$$

In Equation (2.10) LBP features are extracted from red channel (LBP_R), green channel (LBP_G), and blue channel (LBP_B) of RGB space respectively; luminance channel (LBP_Y) and chrominance channels (LBP_U and LBP_V) of YUV space respectively; Hematoxylin channel (LBP_H) and Eosin channel (LBP_E) of HE space [17] respectively; hue channel (LBP_{HH}), saturation channel (LBP_S) and value channel (LBP_{VV}) of HSV space respectively. Resulting feature matrix F_{LBP} is of size 11×128 and fed into the modified PCA algorithm to perform classification and grading of H&E stained liver tissue images.

2.5.1 Experimental Results

The same dataset in Section 2.3 is used which has 454 images of three classes. Classification and grading performance of the modified PCA algorithm using LBP features will be observed and compared with the results obtained by color space features.

As seen in Tables 2.31 and 2.32, designed classifier tends to classify all images as Grade I. Therefore, image classification accuracy is 24.9% and patient classification accuracy is 37.2%. Although almost all of the Grade I images are retrieved

Table 2.31: Confusion Matrix of Three-Class 3-NN Modified PCA Image Classification Using LBP Features

	Grade I	Grade II	Normal	Recall
Grade I	113/119	0/119	6/119	95.0%
Grade II	144/151	0/151	7/151	0.0%
Normal	184/184	0/184	0/184	0.0%
Precision	25.6%	0.0%	0.0%	Overall Accuracy 24.9%

Table 2.32: Confusion Matrix of Three-Class 3-NN Modified PCA Patient Classification Using LBP Features

	Grade I	Grade II	Normal	Recall
Grade I	16/17	0/17	1/17	94.1%
Grade II	16/17	0/17	1/17	0.0%
Normal	9/9	0/9	0/9	0.0%
Precision	39.0%	0.0%	0.0%	Overall Accuracy 37.2%

correctly, Grade I class accuracy is 25.6% due to a high number of false positives. Next, a two-class classification will be performed to classify normal and cancerous liver tissue images.

Table 2.33: Confusion Matrix of Two-Class (Healthy vs. Cancerous) 3-NN Modified PCA Image Classification Using LBP Features

	Cancerous	Normal	Recall
Cancerous	257/270	13/270	95.2%
Normal	184/184	0/184	0.0%
Precision	58.3%	0.0%	Overall Accuracy 56.6%

In Tables 2.33 and 2.34, designed classifier tends to classify all images as cancerous. In this case, image classification accuracy is 56.6% and patient classification accuracy is 74.4%. Almost all of the cancerous images are retrieved correctly, but

Table 2.34: Confusion Matrix of Two-Class (Healthy vs. Cancerous) 3-NN Modified PCA Patient Classification Using LBP Features

	Cancerous	Normal	Recall
Cancerous	32/34	2/34	94.1%
Normal	9/0	0/9	0.0%
Precision	78.0%	0.0%	Overall Accuracy 74.4%

cancerous class accuracy is 58.3% due to a high number of false positives. It is observed that LBP features does not provide meaningful information to distinguish cancerous and normal tissues.

Table 2.35: Confusion Matrix of Two-Class (Grade I vs. Grade II) 3-NN Modified PCA Image Classification Using LBP Features

	Grade I	Grade II	Recall
Grade I	52/119	67/119	43.7%
Grade II	62/151	89/151	58.9%
Precision	45.6%	57.1%	Overall Accuracy 52.2%

Table 2.36: Confusion Matrix of Two-Class (Grade I vs. Grade II) 3-NN Modified PCA Patient Classification Using LBP Features

	Grade I	Grade II	Recall
Grade I	5/17	12/17	29.4%
Grade II	7/17	10/17	58.8%
Precision	41.7%	45.5%	Overall Accuracy 44.1%

In Tables 2.35 and 2.36, cancerous tissues are graded in two-class case. Image classification accuracy is 52.2% and patient classification accuracy is 44.1%. Unlike previous two cases of LBP features, designed classifier does not classify most of the images as a single class. However, classification accuracies are far smaller than the same case with color space features (Tables 2.5, 2.6).

Considering all three cases of classification and grading of H&E stained liver tissue images, it is experimentally observed that LBP features does not extract representative features from normal and cancerous images.

Chapter 3

CSC Classification in H&E Stained Liver Tissue Images Using Directional Feature Extraction Algorithms

In his M.Sc. thesis, Bozkurt introduced directional feature extraction methods for image processing [8]. The purpose of these methods is to extract features of a given image in various directions. In this chapter, directional features from CSC images will be extracted and fed into the modified PCA algorithm for grading classification of H&E stained liver images. Obtained results will be compared with the results in the previous chapter.

3.1 Directional Filtering

Directional filtering framework is developed by Bozkurt in his M.Sc. thesis. In this algorithm, a filter impulse response f_0 and filter length N are set initially. The aim is to filter a given input image in various dimensions. Directional filters

are constructed in several directions and two features are extracted from each direction (mean and standard deviation). Instead of applying directional convolution, directional filters are rotated by θ and convolved with the input image. Rotated filters are calculated as in Bozkurt's thesis. For each directional filter, corresponding rotational filter is calculated by rotating f_0 by θ. Directional and rotated filters for $\theta = \{0°, \pm 26.56°, \pm 45°, \pm 63.43°, 90°\}$ is given in Table 3.1.

Table 3.1: Directional and rotated filters for $\theta = \{0°, \pm 26.56°, \pm 45°, \pm 63.43°, 90°\}$

Angle	Directional Filter	Rotated Filter
$-63.43°$	$\begin{bmatrix} 0 & -0.0313 & -0.0313 & 0 & 0 & 0 & 0 \\ 0 & 0 & 0 & 0 & 0 & 0 & 0 \\ 0 & 0 & 0.2813 & 0.2813 & 0 & 0 & 0 \\ 0 & 0 & 0 & 1 & 0 & 0 & 0 \\ 0 & 0 & 0 & 0.2813 & 0.2813 & 0 & 0 \\ 0 & 0 & 0 & 0 & 0 & 0 & 0 \\ 0 & 0 & 0 & 0 & -0.0313 & -0.0313 & 0 \end{bmatrix}$	$\begin{bmatrix} 0 & -0.01459 & -0.03004 & 0 & 0 & 0 & 0 \\ 0 & -0.00451 & -0.01475 & 0.012539 & 0 & 0 & 0 \\ 0 & 0 & 0.204712 & 0.336475 & 0 & 0 & 0 \\ 0 & 0 & 0.084917 & 1 & 0.084917 & 0 & 0 \\ 0 & 0 & 0 & 0.336475 & 0.204712 & 0 & 0 \\ 0 & 0 & 0 & 0.012539 & -0.01475 & -0.00451 & 0 \\ 0 & 0 & 0 & 0 & -0.03004 & -0.01459 & 0 \end{bmatrix}$
$-45°$	$\begin{bmatrix} -0.0625 & 0 & 0 & 0 & 0 & 0 & 0 \\ 0 & 0 & 0 & 0 & 0 & 0 & 0 \\ 0 & 0 & 0.5625 & 0 & 0 & 0 & 0 \\ 0 & 0 & 0 & 1 & 0 & 0 & 0 \\ 0 & 0 & 0 & 0 & 0.5625 & 0 & 0 \\ 0 & 0 & 0 & 0 & 0 & 0 & 0 \\ 0 & 0 & 0 & 0 & 0 & 0 & -0.0625 \end{bmatrix}$	$\begin{bmatrix} 0 & -0.0085 & 0 & 0 & 0 & 0 & 0 \\ -0.0085 & -0.05178 & -0.00222 & 0 & 0 & 0 & 0 \\ 0 & -0.00222 & 0.329505 & 0.202284 & 0 & 0 & 0 \\ 0 & 0 & 0.202284 & 1 & 0.202284 & 0 & 0 \\ 0 & 0 & 0 & 0.202284 & 0.329505 & -0.00222 & 0 \\ 0 & 0 & 0 & 0 & -0.00222 & -0.05178 & -0.0085 \\ 0 & 0 & 0 & 0 & 0 & -0.0085 & 0 \end{bmatrix}$
$-26.56°$	$\begin{bmatrix} 0 & 0 & 0 & 0 & 0 & 0 & 0 \\ -0.0313 & 0 & 0 & 0 & 0 & 0 & 0 \\ -0.0313 & 0 & 0.2813 & 0 & 0 & 0 & 0 \\ 0 & 0 & 0.2813 & 1 & 0.2813 & 0 & 0 \\ 0 & 0 & 0 & 0 & 0.2813 & 0 & -0.0313 \\ 0 & 0 & 0 & 0 & 0 & 0 & -0.0313 \\ 0 & 0 & 0 & 0 & 0 & 0 & 0 \end{bmatrix}$	$\begin{bmatrix} 0 & 0 & 0 & 0 & 0 & 0 & 0 \\ -0.01459 & -0.00451 & 0 & 0 & 0 & 0 & 0 \\ -0.03004 & -0.01475 & 0.204712 & 0.084917 & 0 & 0 & 0 \\ 0 & 0.012539 & 0.336475 & 1 & 0.336475 & 0.012539 & 0 \\ 0 & 0 & 0 & 0.084917 & 0.204712 & -0.01475 & -0.03004 \\ 0 & 0 & 0 & 0 & 0 & -0.00451 & -0.01459 \\ 0 & 0 & 0 & 0 & 0 & 0 & 0 \end{bmatrix}$
$0°$	$\begin{bmatrix} 0 & 0 & 0 & 0 & 0 & 0 & 0 \\ 0 & 0 & 0 & 0 & 0 & 0 & 0 \\ 0 & 0 & 0 & 0 & 0 & 0 & 0 \\ -0.0625 & 0 & 0.5625 & 1 & 0.5625 & 0 & -0.0625 \\ 0 & 0 & 0 & 0 & 0 & 0 & 0 \\ 0 & 0 & 0 & 0 & 0 & 0 & 0 \\ 0 & 0 & 0 & 0 & 0 & 0 & 0 \end{bmatrix}$	$\begin{bmatrix} 0 & 0 & 0 & 0 & 0 & 0 & 0 \\ 0 & 0 & 0 & 0 & 0 & 0 & 0 \\ 0 & 0 & 0 & 0 & 0 & 0 & 0 \\ -0.0625 & 0 & 0.5625 & 1 & 0.5625 & 0 & -0.0625 \\ 0 & 0 & 0 & 0 & 0 & 0 & 0 \\ 0 & 0 & 0 & 0 & 0 & 0 & 0 \\ 0 & 0 & 0 & 0 & 0 & 0 & 0 \end{bmatrix}$
$26.56°$	$\begin{bmatrix} 0 & 0 & 0 & 0 & 0 & 0 & 0 \\ 0 & 0 & 0 & 0 & 0 & 0 & -0.0313 \\ 0 & 0 & 0 & 0 & 0.2813 & 0 & -0.0313 \\ 0 & 0 & 0.2813 & 1 & 0.2813 & 0 & 0 \\ -0.0313 & 0 & 0.2813 & 0 & 0 & 0 & 0 \\ -0.0313 & 0 & 0 & 0 & 0 & 0 & 0 \\ 0 & 0 & 0 & 0 & 0 & 0 & 0 \end{bmatrix}$	$\begin{bmatrix} 0 & 0 & 0 & 0 & 0 & 0 & 0 \\ 0 & 0 & 0 & 0 & 0 & -0.00451 & -0.01459 \\ 0 & 0 & 0 & 0.084917 & 0.204712 & -0.01475 & -0.03004 \\ 0 & 0.012539 & 0.336475 & 1 & 0.336475 & 0.012539 & 0 \\ -0.03004 & -0.01475 & 0.204712 & 0.084917 & 0 & 0 & 0 \\ -0.01459 & -0.00451 & 0 & 0 & 0 & 0 & 0 \\ 0 & 0 & 0 & 0 & 0 & 0 & 0 \end{bmatrix}$
$45°$	$\begin{bmatrix} 0 & 0 & 0 & 0 & 0 & 0 & -0.0625 \\ 0 & 0 & 0 & 0 & 0 & 0 & 0 \\ 0 & 0 & 0 & 0 & 0.5625 & 0 & 0 \\ 0 & 0 & 0 & 1 & 0 & 0 & 0 \\ 0 & 0 & 0.5625 & 0 & 0 & 0 & 0 \\ 0 & 0 & 0 & 0 & 0 & 0 & 0 \\ -0.0625 & 0 & 0 & 0 & 0 & 0 & 0 \end{bmatrix}$	$\begin{bmatrix} 0 & 0 & 0 & 0 & 0 & -0.0085 & 0 \\ 0 & 0 & 0 & 0 & -0.00222 & -0.05178 & -0.0085 \\ 0 & 0 & 0 & 0.202284 & 0.329505 & -0.00222 & 0 \\ 0 & 0 & 0.202284 & 1 & 0.202284 & 0 & 0 \\ 0 & -0.00222 & 0.329505 & 0.202284 & 0 & 0 & 0 \\ -0.0085 & -0.05178 & -0.00222 & 0 & 0 & 0 & 0 \\ 0 & -0.0085 & 0 & 0 & 0 & 0 & 0 \end{bmatrix}$
$63.43°$	$\begin{bmatrix} 0 & 0 & 0 & 0 & -0.0313 & -0.0313 & 0 \\ 0 & 0 & 0 & 0 & 0 & 0 & 0 \\ 0 & 0 & 0 & 0.2813 & 0.2813 & 0 & 0 \\ 0 & 0 & 0 & 1 & 0 & 0 & 0 \\ 0 & 0 & 0.2813 & 0.2813 & 0 & 0 & 0 \\ 0 & 0 & 0 & 0 & 0 & 0 & 0 \\ 0 & -0.0313 & -0.0313 & 0 & 0 & 0 & 0 \end{bmatrix}$	$\begin{bmatrix} 0 & 0 & 0 & 0 & -0.03004 & -0.01459 & 0 \\ 0 & 0 & 0 & 0.012539 & -0.01475 & -0.00451 & 0 \\ 0 & 0 & 0 & 0.336475 & 0.204712 & 0 & 0 \\ 0 & 0 & 0.084917 & 1 & 0.084917 & 0 & 0 \\ 0 & 0 & 0.204712 & 0.336475 & 0 & 0 & 0 \\ 0 & -0.00451 & -0.01475 & 0.012539 & 0 & 0 & 0 \\ 0 & -0.01459 & -0.03004 & 0 & 0 & 0 & 0 \end{bmatrix}$
$90°$	$\begin{bmatrix} 0 & 0 & 0 & -0.0625 & 0 & 0 & 0 \\ 0 & 0 & 0 & 0 & 0 & 0 & 0 \\ 0 & 0 & 0 & 0.5625 & 0 & 0 & 0 \\ 0 & 0 & 0 & 1 & 0 & 0 & 0 \\ 0 & 0 & 0 & 0.5625 & 0 & 0 & 0 \\ 0 & 0 & 0 & 0 & 0 & 0 & 0 \\ 0 & 0 & 0 & -0.0625 & 0 & 0 & 0 \end{bmatrix}$	$\begin{bmatrix} 0 & 0 & 0 & -0.0625 & 0 & 0 & 0 \\ 0 & 0 & 0 & 0 & 0 & 0 & 0 \\ 0 & 0 & 0 & 0.5625 & 0 & 0 & 0 \\ 0 & 0 & 0 & 1 & 0 & 0 & 0 \\ 0 & 0 & 0 & 0.5625 & 0 & 0 & 0 \\ 0 & 0 & 0 & 0 & 0 & 0 & 0 \\ 0 & 0 & 0 & -0.0625 & 0 & 0 & 0 \end{bmatrix}$

Mean and standard deviations of each directional filter output are used as

features. Therefore, 16 features are obtained from the first scale image for eight directions. In the lower scales, the input image is first decimated by a factor of two both horizontally and vertically. A half sample delay is applied before downsampling, because downsampling operation is shift-variant. After that, the decimated image is filtered by rotated directional filters. Mean and standard deviations of filtered images are used as features. This process can be repeated for further lower scales. At each scale, extracted features constitute a column vector. In multi-scale feature extraction, extracted feature vectors are concatenated to form a 1-D feature vector. In this thesis, features are extracted from three scales that results in a 48 element feature vector for a single input image.

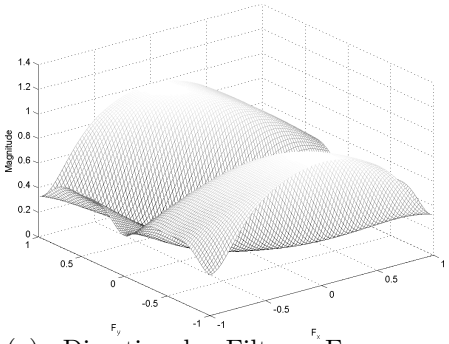

(a) Directional Filter Frequency Response($\theta = -63.43°$)

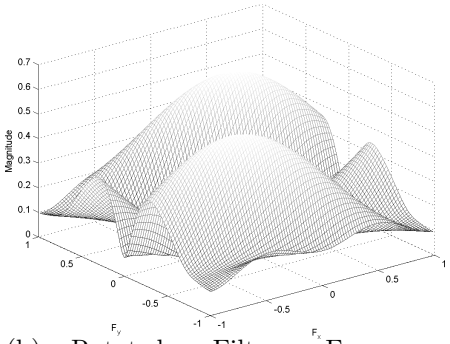

(b) Rotated Filter Frequency Response($\theta = -63.43°$)

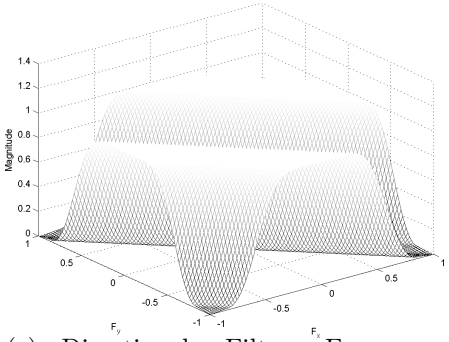

(c) Directional Filter Frequency Response($\theta = -45°$)

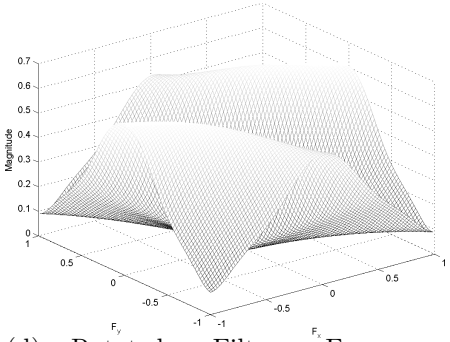

(d) Rotated Filter Frequency Response($\theta = -45°$)

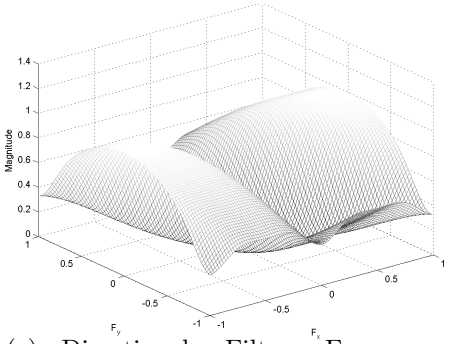

(e) Directional Filter Frequency Response($\theta = -26.56°$)

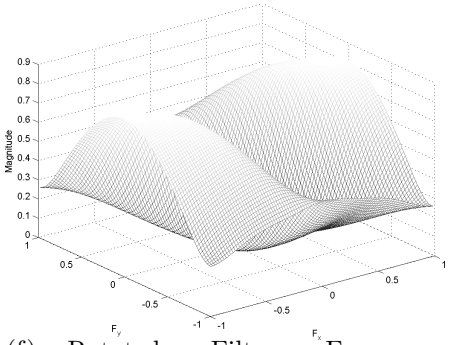

(f) Rotated Filter Frequency Response($\theta = --26.56°$)

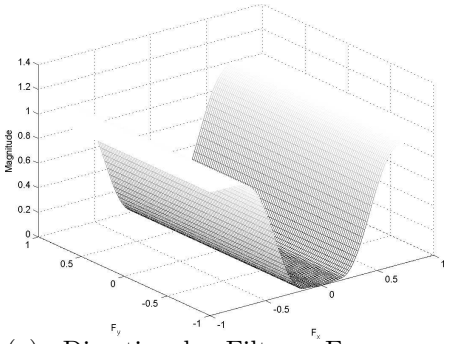

(g) Directional Filter Frequency Response($\theta = 0°$)

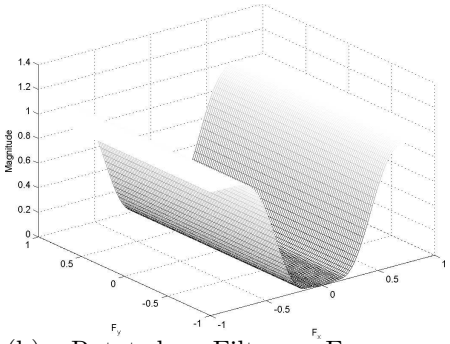

(h) Rotated Filter Frequency Response($\theta = -0°$)

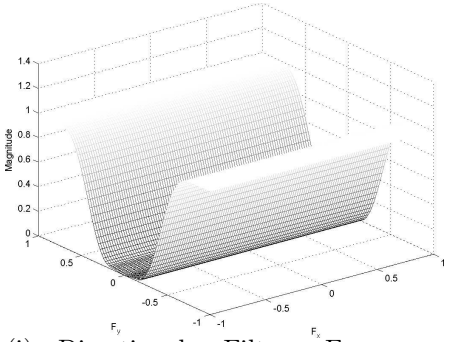

(i) Directional Filter Frequency Response($\theta = 26.56°$)

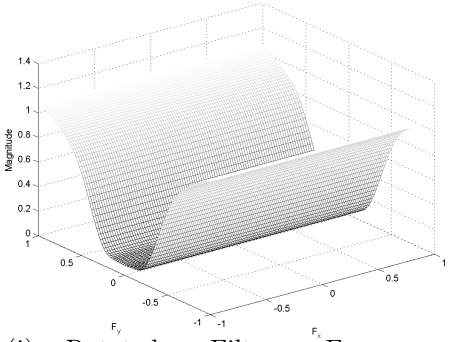

(j) Rotated Filter Frequency Response($\theta = 26.56°$)

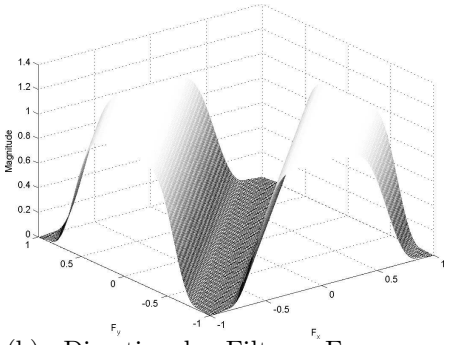

(k) Directional Filter Frequency Response($\theta = 45°$)

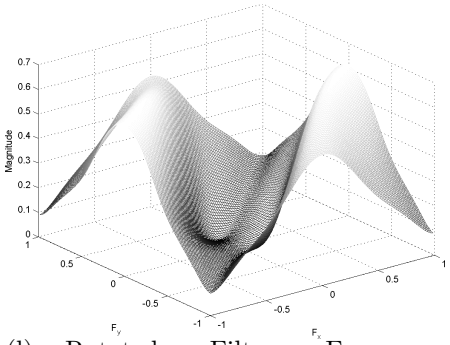

(l) Rotated Filter Frequency Response($\theta = 45°$)

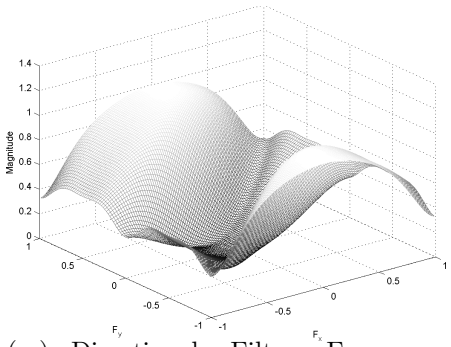

(m) Directional Filter Frequency Response($\theta = 63.43°$)

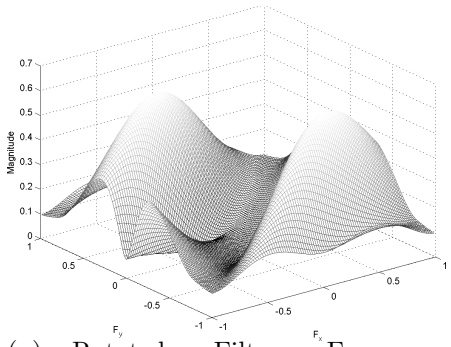

(n) Rotated Filter Frequency Response($\theta = 63.43°$)

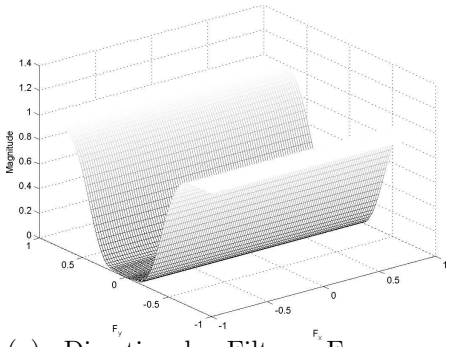

(o) Directional Filter Frequency Response($\theta = 90°$)

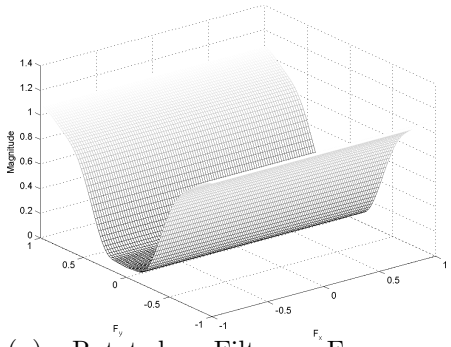

(p) Rotated Filter Frequency Response($\theta = 90°$)

Figure 3.1: Frequency responses of directional and rotated filters, for $\theta = 0°, \pm 26.56°, \pm 45°, \pm 63.43°, 90°$

3.2 Experimental Results

In the experiments, features are extracted from three color channels, three scales, eight directions ($\theta = \{0°, \pm 26.56°, \pm 45°, \pm 63.43°, 90°\}$) and low-pass filter is $f_l = [0.25 \quad 0.5 \quad 0.25]$.

$$F_{dir} = [\mathbf{D}_R \quad \mathbf{D}_G \quad \mathbf{D}_B]^T \tag{3.1}$$

,where $\mathbf{D}_R$ is features extracted from red channel, $\mathbf{D}_G$ is features extracted from green channel, $\mathbf{D}_B$ is features extracted from blue channel of RGB color space respectively. Therefore, resulting feature matrix F_{dir} is of size 3×48 and fed into the modified PCA algorithm for grading classification of H&E images.

Table 3.2: Confusion Matrix of Three-Class 3-NN Modified PCA Image Classification with Directional Filtering Features Extracted from 3 Scales

	Grade I	Grade II	Normal	Recall
Grade I	48/119	52/119	19/119	40.3%
Grade II	64/151	43/151	44/151	28.5%
Normal	22/184	46/184	116/184	63.0%
Precision	35.8%	30.5%	64.8%	Overall Accuracy 45.6%

Table 3.3: Confusion Matrix of Three-Class 3-NN Modified PCA Patient Classification with Directional Filtering Features Extracted from 3 Scales

	Grade I	Grade II	Normal	Recall
Grade I	8/17	7/17	2/17	47.1%
Grade II	9/17	4/17	4/17	23.5%
Normal	1/9	0/9	8/9	88.9%
Precision	44.4%	36.3%	57.1%	Overall Accuracy 46.5%

In three-class case, directional filtering features (Tables 3.2 and 3.3) produce accuracies smaller than the accuracies obtained by the color space features in the previous chapter (Tables 2.1 and 2.2). In this case, the best recognition

is achieved in normal class images. Normal images can be classified at 64.8% accuracy.

Table 3.4: Confusion Matrix of Two-Class (Cancerous vs. Normal) 3-NN Modified PCA Image Classification with Directional Filtering Features Extracted from 3 Scales

	Cancerous	Normal	Recall
Cancerous	213/270	57/270	78.9%
Normal	73/184	111/184	60.3%
Precision	74.5%	66.1%	Overall Accuracy 71.4%

Table 3.5: Confusion Matrix of Two-Class (Cancerous vs. Normal) 3-NN Modified PCA Patient Classification with Directional Filtering Features Extracted from 3 Scales

	Cancerous	Normal	Recall
Cancerous	28/34	6/34	82.4%
Normal	2/9	7/9	77.8%
Precision	93.3%	53.8%	Overall Accuracy 81.4%

In two-class 'cancerous or not' classification, accuracies obtained by directional filtering features (Tables 3.4 and 3.5) are comparable to the accuracies obtained by the color space features in the previous chapter (Tables 2.3 and 2.4). Overall image classification accuracy is 71.4% and overall patient classification is 81.4%.

Two-class grading classification results of cancerous images are presented in Tables 3.6 and 3.7. In this case, classification accuracies are smaller than the accuracies obtained by the color space features in the previous chapter (Tables 2.5 and 2.6). Classification accuracies are close to 50% and the best classification performance is observed in Grade II image classification.

It is experimentally observed that directional features do not produce good detection results because H&E stained liver tissue images are not directional features.

Table 3.6: Confusion Matrix of Two-Class (Grade I vs. Grade II) 3-NN Modified PCA Image Classification with Directional Filtering Features Extracted from 3 Scales

	Grade I	Grade II	Recall
Grade I	55/119	64/119	46.2%
Grade II	74/151	77/151	51.0%
Precision	42.6%	54.6%	Overall Accuracy 48.9%

Table 3.7: Confusion Matrix of Two-Class (Grade I vs. Grade II) 3-NN Modified PCA Patient Classification with Directional Filtering Features Extracted from 3 Scales

	Grade I	Grade II	Recall
Grade I	8/17	9/17	47.1%
Grade II	9/17	8/17	47.1%
Precision	47.1%	47.1%	Overall Accuracy 47.1%

Chapter 4

Modified PCA Algorithm Based CSC Classification Using Multiplication-free Cosine-Like Similarity Measures

A well-known convex cost function is the ℓ_1 norm function $f(\mathbf{x}) = ||\mathbf{x}||_1$. Its gradient leads to a widely used correlation measure based on the sign information of input vectors:

$$SG(\mathbf{x}) = [\text{sign}(x_1), \text{sign}(x_2), \ldots, \text{sign}(x_N)]^T \tag{4.1}$$

In this case, the cosine similarity function is normalized by the ℓ_2 norms of the above gradient vectors:

$$c0(\mathbf{x}, \mathbf{y}) \triangleq \frac{\sum_{i=1}^{N} (SG(\mathbf{x}))_i \times (SG(\mathbf{y}))_i}{\|SG(\mathbf{x})\|_2 \times \|SG(\mathbf{y})\|_2} \tag{4.2}$$

This similarity vector is too simple for many applications. For $c0$ similarity

measure, the similarity between two vectors in the third step (2.5) of the modified PCA algorithm is replaced by the following operation:

$$sim(I_1, I_2) = c0(\boldsymbol{v}, \boldsymbol{w}) = \frac{\sum_{i=1}^{N} (SG(\boldsymbol{v}))_i \times (SG(\boldsymbol{w}))_i}{\|SG(\boldsymbol{v})\|_2 \times \|SG(\boldsymbol{w})\|_2} \tag{4.3}$$

We recently introduced a related family of multiplication-free vector products [33–39]. It is based on an additive operator whose sign is the same as the multiplication. Let a and b be two real numbers. The new operator $\odot$ is defined as follows:

$$a \odot b = sign(a \times b) \cdot (|a| + |b|), \tag{4.4}$$

where

$$sign(a \times b) = \begin{cases} 1, & \text{if } a \cdot b > 0, \\ 0, & \text{if } a \cdot b = 0, \\ -1, & \text{if } a \cdot b < 0. \end{cases} \tag{4.5}$$

The operator $\odot$ is basically a summation operation. However, the sign of the result of $a \odot b$ is the same as $a \times b$. Therefore, the $\odot$ operator behaves like the multiplication operation.

We define a new "vector product" of two N-dimensional vectors $\mathbf{x}_1$ and $\mathbf{x}_2$ based on $\odot$ in R^N as follows:

$$< \mathbf{x}_1 \odot \mathbf{x}_2 >= \sum_{i=1}^{N} x_1(i) \odot x_2(i), \tag{4.6}$$

,where $x_1(i)$ and $x_2(i)$ are the i-th elements of the vectors $\mathbf{x}_1$ and $\mathbf{x}_2$, respectively. Notice that the vector product of a vector $\mathbf{x}$ with itself reduces to a scaled l_1 norm of $\mathbf{x}$ as follows:

$$< \mathbf{x} \odot \mathbf{x} >= \sum_{i=1}^{N} x(i) \odot x(i) = 2 \sum_{i=1}^{N} |x(i)| = 2||\mathbf{x}||_1. \tag{4.7}$$

Based on the new vector product, we define several vector similarity measures between the two vectors x and y as follows:

$$c1(\mathbf{x}, \mathbf{y}) \triangleq \frac{< \mathbf{x} \odot \mathbf{y} >}{\|\mathbf{x}\|_1 + \|\mathbf{y}\|_1}, \tag{4.8}$$

where $\|\mathbf{x}\|_1$ and $\|\mathbf{y}\|_1$ are the ℓ_1 norms of vectors $\mathbf{x}$ and $\mathbf{y}$, respectively. Similar to the ordinary cosine similarity measure, the numerator contains the vector product of the two vectors and the vector product is normalized by the sum of the ℓ_1 norms of the two vectors $\mathbf{x}$ and $\mathbf{y}$. When $\mathbf{x} = \mathbf{y}$, $c1(\mathbf{x}, \mathbf{y}) = 1$ because $< \mathbf{x} \odot \mathbf{x} > = 2\|\mathbf{x}\|_1$.

According to the definition of the $c1$ similarity measure, the similarity between two vectors in the third step (2.5) of the modified PCA algorithm is replaced by the following operation:

$$sim(I_1, I_2) = c1(\boldsymbol{v}, \boldsymbol{w}) = \frac{< \boldsymbol{v} \odot \boldsymbol{w} >}{\|\boldsymbol{v}\|_1 + \|\boldsymbol{w}\|_1} \tag{4.9}$$

It is also possible to define other related measures using relation operators:

$$c2(\mathbf{x}, \mathbf{y}) \triangleq \frac{\sum_{i=1}^{N} sign(x_i \times y_i) \cdot max(|x_i|, |y_i|)}{(\|\mathbf{x}\|_1 + \|\mathbf{y}\|_1)/2}, \tag{4.10}$$

where $sign(x_i \times y_i)$ is defined as in (4.5) and the vectors $\mathbf{x} = [x_1, x_2, ..., x_N]^T$ and $\mathbf{y} = [y_1,\ y_2,\ ...\ ,\ y_N]^T$, respectively. By using the $c2$ similarity measure, the similarity between two vectors in the third step (2.5) of the modified PCA algorithm is replaced by the following operation:

$$sim(I_1, I_2) = c2(\boldsymbol{v}, \boldsymbol{w}) = \frac{\sum_{i=1}^{N} sign(v_i \times w_i) \cdot max(|v_i|, |w_i|)}{(\|\boldsymbol{v}\|_1 + \|\boldsymbol{w}\|_1)/2} \tag{4.11}$$

A related fourth cosine similarity measure is defined as follows:

$$c3(\mathbf{x},\mathbf{y}) \triangleq \frac{\sum_{i=1}^{N} sign(x_i \times y_i) \cdot min(|x_i|,|y_i|)}{(\|\mathbf{x}\|_1 + \|\mathbf{y}\|_1)/2} \tag{4.12}$$

,where the maximum operation in (4.10) is replaced by the minimum operation. By employing the $c3$ similarity measure, the similarity between two vectors in the third step (2.5) of the modified PCA algorithm is replaced by the following operation:

$$sim(I_1, I_2) = c3(\boldsymbol{v},\boldsymbol{w}) = \frac{\sum_{i=1}^{N} sign(v_i \times w_i) \cdot min(|v_i|,|w_i|)}{(\|\boldsymbol{v}\|_1 + \|\boldsymbol{w}\|_1)/2} \tag{4.13}$$

The similarity measure $c1$ can also be normalized in a different manner as follows:

$$c4(\mathbf{x},\mathbf{y}) \triangleq \frac{< \mathbf{x} \odot \mathbf{y} >}{2 \cdot \sum_{i=1}^{N} max(|x_i|,|y_i|)} \tag{4.14}$$

Clearly, when $\mathbf{x} = \mathbf{y}$, $c4(\mathbf{x},\mathbf{x}) = 1$. Similarly, $c2$ and $c3$ can also be normalized as in $c4$. By utilizing the $c4$ similarity measure, the similarity between two vectors in the third step (2.5) of the modified PCA algorithm is replaced by the following operation:

$$sim(I_1, I_2) = c4(\boldsymbol{v},\boldsymbol{w}) = \frac{< \mathbf{v} \odot \mathbf{w} >}{2 \cdot \sum_{i=1}^{N} max(|v_i|,|w_i|)} \tag{4.15}$$

In all proposed similarity measures defined in Equations 4.2, 4.8, 4.10, 4.12 and 4.14, the term $sign(x_i \times y_i)$ is common and provides the correlation information between the two vectors $\mathbf{x}$ and $\mathbf{y}$. As a result, the computational complexity and power consumption due to signal analysis can be decreased significantly.

Obviously, $ci(\mathbf{x},\mathbf{y}) = ci(\mathbf{y},\mathbf{x}), \quad i = 0,1,2,3,4$ in all three definitions [38–41]. Also, when $\mathbf{x}$=$\mathbf{y}$, they all produce the same result, i.e., $c0(\mathbf{x},\mathbf{y}) = c1(\mathbf{x},\mathbf{y}) =$

$c2(\mathbf{x},\mathbf{y}) = c3(\mathbf{x},\mathbf{y}) = c4(\mathbf{x},\mathbf{y}) = 1$. Multiplication requires more power than addition and relational *max* or *min* operations. Since all five measures can be computed without performing any multiplications, they are all low-power vector similarity measures.

4.1 Experimental Results

In the experiments, proposed cosine-like similarity measures are employed in the modified PCA method. The same dataset in Section 2.3 is used. Features are extracted from color spaces and the same feature matrix in Chapter 2 is used. Classification performance of the proposed similarity measures are compared to the ordinary cosine similarity measure by employing them in the modified PCA algorithm.

4.1.1 Results with $c0$ Similarity Measure

Table 4.1: Confusion Matrix of Three-Class 3-NN $c0$ Similarity Measure Based Modified PCA Image Classification

	Grade I	Grade II	Normal	Recall
Grade I	64/119	41/119	14/119	53.8%
Grade II	67/151	79/151	5/151	52.3%
Healthy	42/184	13/184	129/184	70.1%
Precision	37.0%	59.4%	87.2%	Overall Accuracy 59.9%

As seen in Tables 4.1, 4.2, $c0$ similarity measure produces comparable results to the ordinary cosine similarity measure (Tables 2.1, 2.2) in three-class image and patient classification. Precision of normal images is 87.2% (Table 4.1), which is very close to the results obtained by the ordinary cosine similarity.

In two-class 'cancerous or not' classification, $c0$ similarity measure produces

Table 4.2: Confusion Matrix of Three-Class 3-NN $c0$ Similarity Measure Based Modified PCA Patient Classification

	Grade I	Grade II	Normal	Recall
Grade I	11/17	4/17	2/17	64.7%
Grade II	6/17	10/17	1/17	58.8%
Healthy	2/9	0/9	7/9	77.8%
Precision	57.9%	71.4%	70.0%	Overall Accuracy 65.1%

Table 4.3: Confusion Matrix of Two-Class (Cancerous vs. Normal) 3-NN $c0$ Similarity Measure Based Modified PCA Image Classification

	Cancerous	Normal	Recall
Cancerous	251/270	19/270	93.0%
Normal	55/184	129/184	70.1%
Precision	82.0%	87.2%	Overall Accuracy 83.7%

83.7% classification accuracy in image classification and 88.4% classification accuracy in patient classification. These results (Tables 4.3, 4.4) are comparable to the ordinary cosine similarity measure (Tables 2.3, 2.4). Similar to the three-class case, the closest performance to the ordinary cosine similarity measure is obtained in normal image classification (Table 4.3).

In two-class grading classification of cancerous images, $c0$ similarity measure produces comparable results (Tables 4.5, 4.6) to the ordinary cosine similarity measure (Tables 2.5, 2.6). The closest performance to the ordinary cosine similarity measure is obtained in Grade II patient classification (Table 4.6).

To summarize, $c0$ similarity measure cannot produce better results than the ordinary cosine similarity measure. However, performance of $c0$ similarity measure is comparable to the ordinary cosine similarity measure in all cases.

Table 4.4: Confusion Matrix of Two-Class (Cancerous vs. Normal) 3-NN $c0$ Similarity Measure Based Modified PCA Patient Classification

	Cancerous	Normal	Recall
Cancerous	31/34	3/34	91.2%
Normal	2/9	7/9	77.8%
Precision	93.9%	70.0%	Overall Accuracy 88.4%

Table 4.5: Confusion Matrix of Two-Class (Grade I vs. Grade II) 3-NN $c0$ Similarity Measure Based Modified PCA Image Classification

	Grade I	Grade II	Recall
Grade I	76/119	43/119	63.9%
Grade II	58/151	93/151	38.4%
Precision	56.7%	68.4%	Overall Accuracy 62.6%

Table 4.6: Confusion Matrix of Two-Class (Grade I vs. Grade II) 3-NN $c0$ Similarity Measure Based Modified PCA Patient Classification

	Grade I	Grade II	Recall
Grade I	12/17	5/17	70.6%
Grade II	7/17	10/17	58.8%
Precision	63.2%	66.7%	Overall Accuracy 64.7%

4.1.2 Results with $c1$ Similarity Measure

Table 4.7: Confusion Matrix of Three-Class 3-NN $c1$ Similarity Measure Based Modified PCA Image Classification

	Grade I	Grade II	Healthy	Recall
Grade I	42/119	58/119	19/119	35.3%
Grade II	47/151	98/151	6/151	64.9%
Healthy	26/184	5/184	153/184	83.2%
Precision	36.5%	60.9%	86.0%	Overall Accuracy 64.5%

Table 4.8: Confusion Matrix of Three-Class 3-NN $c1$ Similarity Measure Based Modified PCA Patient Classification

	Grade I	Grade II	Healthy	Recall
Grade I	6/17	8/17	3/17	35.3%
Grade II	5/17	11/17	1/17	64.7%
Healthy	1/9	0/9	8/9	88.9%
Precision	50.0%	57.9%	66.7%	Overall Accuracy 58.1%

As seen in Tables 4.7, 4.8, $c1$ similarity measure produces comparable results to the ordinary cosine similarity measure (Tables 2.1, 2.2) in three-class image and patient classification. Similar to the $c0$ similarity measure based three-class classification (Table 4.1), the closest performance to the ordinary cosine similarity measure is obtained in normal image classification (Table 4.7).

In two-class 'cancerous or not' classification, $c1$ similarity measure produces 86.8% image classification accuracy and 88.4% patient classification accuracy. These results (Tables 4.9, 4.10) are comparable to the ordinary cosine similarity measure (Tables 2.3, 2.4). The closest accuracy to the ordinary cosine similarity measure is observed in cancerous patient classification (Table 4.10).

In two-class grading classification of cancerous images, $c1$ similarity measure produces 72.2% in image classification and 76.5% accuracy in patient classification

Table 4.9: Confusion Matrix of Two-Class (Cancerous vs. Normal) 3-NN $c1$ Similarity Measure Based Modified PCA Image Classification

	Cancerous	Normal	Recall
Cancerous	246/270	24/270	91.1%
Normal	36/184	148/184	80.4%
Precision	87.2%	86.0%	Overall Accuracy 86.8%

Table 4.10: Confusion Matrix of Two-Class (Cancerous vs. Normal) 3-NN $c1$ Similarity Measure Based Modified PCA Patient Classification

	Cancerous	Normal	Recall
Cancerous	30/34	4/34	88.2%
Normal	1/9	8/9	88.9%
Precision	96.8%	66.7%	Overall Accuracy 88.4%

(Tables 4.11, 4.12). These accuracies are better than the accuracies obtained by the ordinary cosine similarity measure (Tables 2.5, 2.6).

Briefly, $c1$ similarity measure can produce results similar to the ordinary cosine similarity measure. Moreover, $c1$ similarity measure outperforms the ordinary cosine similarity measure in two-class grading classification of cancerous images.

Table 4.11: Confusion Matrix of Two-Class (Grade I vs. Grade II) 3-NN $c1$ Similarity Measure Based Modified PCA Image Classification

	Grade I	Grade II	Recall
Grade I	73/119	46/119	61.3%
Grade II	29/151	122/151	80.8%
Precision	71.6%	72.6%	Overall Accuracy 72.2%

Table 4.12: Confusion Matrix of Two-Class (Grade I vs. Grade II) 3-NN $c1$ Similarity Measure Based Modified PCA Patient Classification

	Grade I	Grade II	Recall
Grade I	11/17	6/17	64.7%
Grade II	2/17	15/17	88.2%
Precision	84.6%	71.4%	Overall Accuracy 76.5%

4.1.3 Results with $c2$ Similarity Measure

Table 4.13: Confusion Matrix of Three-Class 3-NN $c2$ Similarity Measure Based Modified PCA Image Classification

	Grade I	Grade II	Healthy	Recall
Grade I	20/119	45/119	54/119	16.8%
Grade II	54/151	62/151	35/151	41.1%
Healthy	65/184	16/184	103/184	56.0%
Precision	14.4%	50.4%	53.6%	Overall Accuracy 40.8%

As seen in Tables 4.13, 4.14, $c2$ similarity measure cannot produce meaningful results compared to the ordinary cosine similarity measure (Tables 2.1, 2.2) in three-class image and patient classification.

In two-class 'cancerous or not' classification, $c2$ similarity measure produces 63.2% image classification accuracy and 62.8% patient classification accuracy.

Table 4.14: Confusion Matrix of Three-Class 3-NN $c2$ Similarity Measure Based Modified PCA Patient Classification

	Grade I	Grade II	Healthy	Recall
Grade I	3/17	7/17	7/17	17.6%
Grade II	7/17	6/17	4/17	35.3%
Healthy	4/9	0/9	5/9	55.6%
Precision	21.4%	46.2%	31.2%	Overall Accuracy 32.6%

Table 4.15: Confusion Matrix of Two-Class (Cancerous vs. Normal) 3-NN $c2$ Similarity Measure Based Modified PCA Image Classification

	Cancerous	Normal	Recall
Cancerous	186/270	84/270	68.9%
Normal	83/184	101/184	54.9%
Precision	69.1%	54.6%	Overall Accuracy 63.2%

These accuracies (Tables 4.15, 4.16) are far smaller than the ordinary cosine similarity measure (Tables 2.3, 2.4). In this case, classification accuracy of normal images are significantly smaller than cancerous images. In Table 4.16, classification accuracy of cancerous patients is comparable to the ordinary cosine similarity (Table 2.4).

In two-class grading classification of cancerous images, $c2$ similarity measure cannot produce meaningful results (Tables 4.17, 4.18) compared to the ordinary cosine similarity measure (Tables 2.5, 2.6).

Succinctly, $c2$ similarity measure cannot produce better results than the ordinary cosine similarity measure. In all cases, $c2$ similarity measure classifies images at low accuracy levels.

Table 4.16: Confusion Matrix of Two-Class (Cancerous vs. Normal) 3-NN $c2$ Similarity Measure Based Modified PCA Patient Classification

	Cancerous	Normal	Recall
Cancerous	22/34	12/34	64.7%
Normal	4/9	5/9	55.6%
Precision	84.6%	29.4%	Overall Accuracy 62.8%

Table 4.17: Confusion Matrix of Two-Class (Grade I vs. Grade II) 3-NN $c2$ Similarity Measure Based Modified PCA Image Classification

	Grade I	Grade II	Recall
Grade I	19/119	100/119	16.0%
Grade II	68/151	83/151	55.0%
Precision	21.8%	45.4%	Overall Accuracy 37.8%

Table 4.18: Confusion Matrix of Two-Class (Grade I vs. Grade II) 3-NN $c2$ Similarity Measure Based Modified PCA Patient Classification

	Grade I	Grade II	Recall
Grade I	1/17	16/17	5.9%
Grade II	8/17	9/17	52.9%
Precision	11.1%	36.0%	Overall Accuracy 29.4%

4.1.4 Results with $c3$ Similarity Measure

Table 4.19: Confusion Matrix of Three-Class 3-NN $c3$ Similarity Measure Based Modified PCA Image Classification

	Grade I	Grade II	Healthy	Recall
Grade I	65/119	39/119	15/119	54.6%
Grade II	35/151	104/151	12/151	68.9%
Healthy	7/184	3/184	174/184	94.6%
Precision	60.7%	71.2%	86.6%	Overall Accuracy 75.6%

Table 4.20: Confusion Matrix of Three-Class 3-NN $c3$ Similarity Measure Based Modified PCA Patient Classification

	Grade I	Grade II	Healthy	Recall
Grade I	10/17	5/17	2/17	58.8%
Grade II	4/17	11/17	2/17	64.7%
Healthy	0/9	0/9	9/9	100%
Precision	71.4%	68.8%	69.2%	Overall Accuracy 69.8%

As seen in Table 4.19, $c3$ similarity measure outperforms the ordinary cosine similarity measure (Table 2.1) in three-class image classification. Three-class patient classification accuracy of $c3$ similarity measure (Table 4.20) is very close to the accuracy obtained by the ordinary cosine similarity measure (Table 2.2).

In two-class 'cancerous or not' classification, $c3$ similarity measure produces 91.6% image classification accuracy and 90.7% patient classification accuracy. These results (Tables 4.21, 4.22) are very close to the results obtained by the ordinary cosine similarity measure (Tables 2.3, 2.4). In Table 4.21, $c3$ similarity measure surpasses the ordinary cosine similarity measure (Table 2.3) in classification of cancerous images.

In two-class grading classification of cancerous images, $c3$ similarity measure produces results (Table 4.23) very close to the results obtained by the ordinary

Table 4.21: Confusion Matrix of Two-Class (Cancerous vs. Normal) 3-NN $c3$ Similarity Measure Based Modified PCA Image Classification

	Cancerous	Normal	Recall
Cancerous	243/270	27/270	90.0%
Normal	10/184	174/184	94.6%
Precision	96.0%	86.6%	Overall Accuracy 91.6%

Table 4.22: Confusion Matrix of Two-Class (Cancerous vs. Normal) 3-NN $c3$ Similarity Measure Based Modified PCA Patient Classification

	Cancerous	Normal	Recall
Cancerous	30/34	4/34	88.2%
Normal	0/9	9/9	100%
Precision	100%	69.2%	Overall Accuracy 90.7%

cosine similarity measure (Table 2.5). In patient classification of the same case, $c3$ similarity measure (Table 4.24) performs the same as the ordinary cosine similarity measure (Table 2.6).

Briefly, $c3$ similarity measure cannot produce better results than the ordinary cosine similarity measure. However, in all cases performance of $c3$ similarity measure is comparable to the ordinary cosine similarity measure.

Table 4.23: Confusion Matrix of Two-Class (Grade I vs. Grade II) 3-NN $c3$ Similarity Measure Based Modified PCA Image Classification

	Grade I	Grade II	Recall
Grade I	74/119	45/119	62.2%
Grade II	38/151	113/151	74.8%
Precision	66.1%	71.5%	Overall Accuracy 69.3%

Table 4.24: Confusion Matrix of Two-Class (Grade I vs. Grade II) 3-NN $c3$ Similarity Measure Based Modified PCA Patient Classification

	Grade I	Grade II	Recall
Grade I	11/17	6/17	64.7%
Grade II	3/17	14/17	82.4%
Precision	78.6%	70.0%	Overall Accuracy 73.5%

4.1.5 Results with $c4$ Similarity Measure

Table 4.25: Confusion Matrix of Three-Class 3-NN $c4$ Similarity Measure Based Modified PCA Image Classification

	Grade I	Grade II	Healthy	Recall
Grade I	61/119	42/119	16/119	51.2%
Grade II	35/151	109/151	7/151	72.2%
Healthy	4/184	5/184	175/184	95.1%
Precision	61.0%	69.9%	88.4%	Overall Accuracy 76.0%

As seen in Table 4.25, $c4$ similarity measure outperforms the ordinary cosine similarity measure (Table 2.1) in three-class image classification. In patient classification of the same case, $c4$ similarity measure (Table 4.26) produces results very close to the results obtained by the ordinary cosine similarity measure (Table 2.2).

In two-class 'cancerous or not' classification, $c4$ similarity measure produces

Table 4.26: Confusion Matrix of Three-Class 3-NN $c4$ Similarity Measure Based Modified PCA Patient Classification

	Grade I	Grade II	Healthy	Recall
Grade I	10/17	6/17	1/17	58.8%
Grade II	4/17	12/17	1/17	70.6%
Healthy	0/9	0/9	9/9	100%
Precision	71.4%	66.7%	81.8%	Overall Accuracy 72.1%

Table 4.27: Confusion Matrix of Two-Class (Cancerous vs. Normal) 3-NN $c4$ Similarity Measure Based Modified PCA Image Classification

	Cancerous	Normal	Recall
Cancerous	248/270	22/270	91.9%
Normal	10/184	174/184	94.6%
Precision	96.1%	88.8%	Overall Accuracy 93.0%

93.0% image classification accuracy and 90.7% patient classification accuracy. In image classification, $c4$ similarity measure (Table 4.27) outperforms the ordinary cosine similarity measure (Table 2.3). In patient classification of the same case, $c4$ similarity measure (Table 4.28) produces results very similar to the results obtained by the ordinary cosine similarity measure (Table 2.4).

In two-class grading classification of cancerous images, $c4$ similarity measure surpasses (Tables 4.29, 4.30) the ordinary cosine similarity measure (Tables 2.5, 2.6) in both image and patient classification.

Succinctly, $c4$ similarity measure produces results very close to the results obtained by the ordinary cosine similarity measure. Furthermore, performance of $c4$ similarity measure is better than the ordinary cosine similarity measure in some cases.

Table 4.28: Confusion Matrix of Two-Class (Cancerous vs. Normal) 3-NN $c4$ Similarity Measure Based Modified PCA Patient Classification

	Cancerous	Normal	Recall
Cancerous	30/34	4/34	88.2%
Normal	0/9	9/9	100%
Precision	100%	69.2%	Overall Accuracy 90.7%

Table 4.29: Confusion Matrix of Two-Class (Grade I vs. Grade II) 3-NN $c4$ Similarity Measure Based Modified PCA Image Classification

	Grade I	Grade II	Recall
Grade I	81/119	38/119	68.1%
Grade II	33/151	118/151	78.1%
Precision	71.1%	75.6%	Overall Accuracy 73.7%

Table 4.30: Confusion Matrix of Two-Class (Grade I vs. Grade II) 3-NN $c4$ Similarity Measure Based Modified PCA Patient Classification

	Grade I	Grade II	Recall
Grade I	12/17	5/17	70.6%
Grade II	3/17	14/17	82.4%
Precision	80.0%	73.7%	Overall Accuracy 76.5%

4.1.6 Summary

In this subsection, overall classification accuracies of the proposed similarity measures and the ordinary cosine similarity in three cases are presented.

Table 4.31: Overall 3-NN Image Classification Accuracies Using Modified PCA Method with 6 Different Similarity Measures. Best Result in Each Case is Presented in Bold Fonts.

	3 Class	2 Class (Cancerous vs. Normal)	2 Class (Grade I vs. Grade II)
cosine	74.7%	92.1%	70.4%
c0	59.9%	83.7%	62.6%
c1	64.5%	86.8%	72.2%
c2	40.8%	63.2%	37.8%
c3	75.6%	91.6%	69.3%
c4	**76.0**%	**93.0**%	**73.7**%

Table 4.32: Overall 3-NN Patient Classification Accuracies Using Modified PCA Method with 6 Different Similarity Measures. Best Result in Each Case is Presented in Bold Fonts.

	3 Class	2 Class (Cancerous vs. Normal)	2 Class (Grade I vs. Grade II)
cosine	**74.4**%	**93.0**%	73.5%
c0	65.1%	88.4%	64.7%
c1	58.1%	88.4%	**76.5**%
c2	32.6%	62.8%	29.4%
c3	69.8%	90.7%	73.5%
c4	72.1%	90.7%	**76.5**%

As seen in Tables 4.31 and 4.32, $c4$ similarity measure gives the best results in four of six cases. It performs the best classification in all cases of image classification among six similarity measures. Proposed $c1$ similarity measure produces the same best result as $c4$ similarity measure in two-class Grade I vs. Grade II patient classification. Remaining two best classification accuracies are achieved

with the ordinary cosine similarity measure.

Proposed $c1$ similarity measure also produces the second best result and performs better than the ordinary cosine similarity measure in two-class Grade I vs. Grade II image classification. Proposed $c3$ similarity measure produces the second best result and performs better than the ordinary cosine similarity measure in three-class image classification.

4.2 Application on H&E Stained Lung Tissue Image Dataset

We also have a dataset containing two classes of H&E stained lung tissue images; Grade I (128 images taken from 16 patients) and Grade II (208 images taken from 26 patients). Similar to the previous experiments, we use three-nearest neighbor classification by following leave-one-patient-out strategy instead of leave-one-image-out strategy. The test set is circulated to cover all instances and contains one image at each iteration. We utilize only color space features and $c4$ similarity measure based modified PCA algorithm for classification in order to show that this proposed classification algorithm can also produce good results on H&E stained lung tissue images.

Table 4.33: Confusion Matrix of Two-Class (Grade I vs. Grade II) 3-NN $c4$ Similarity Measure Based Modified PCA Image Classification

	Grade I	Grade II	Recall
Grade I	76/128	52/128	59.4%
Grade II	53/208	155/208	74.5%
Precision	58.9%	74.9%	Overall Accuracy 68.9%

In two-class grading classification of H&E stained cancerous lung tissue images, 68.9% image classification accuracy and 78.6% patient classification accuracy are obtained (Tables 4.33, 4.34). Image classification accuracy on lung dataset is very

Table 4.34: Confusion Matrix of Two-Class (Grade I vs. Grade II) 3-NN $c4$ Similarity Measure Based Modified PCA Patient Classification

	Grade I	Grade II	Recall
Grade I	11/16	5/16	68.8%
Grade II	4/26	22/26	84.6%
Precision	73.3%	81.5%	Overall Accuracy 78.6%

close to the image classification accuracy obtained in liver dataset by utilizing the same classification algorithm and feature extraction method (presented in Section 4.1.5, Table 4.29). In patient classification, classification accuracies obtained on lung dataset are better than the classification accuracies obtained on liver dataset by using the same classification algorithm and feature extraction method (presented in Section 4.1.5, Table 4.30).

It is experimentally shown that it is also possible to achieve good classification accuracies on H&E stained lung tissue images by utilizing the proposed modified PCA algorithm.

Chapter 5

Conclusion

In this thesis, we propose a modified version of PCA algorithm that uses covariance matrices of feature matrices instead of pixel values of images in order to classify and grade H&E stained liver tissue images. Our main challenge is to grade images according to their CSC ratios, while CSCs cannot be observed by naked eye in H&E stained tissues. This fact makes us choose features meticulously and develop a proper classification algorithm.

We present an efficient classification algorithm that can classify and grade H&E stained liver tissue images. Our main motivation is to make a classification based on texture differences. Therefore, 20 features are extracted from nine different color channels. In the proposed PCA algorithm, covariance matrix of the feature matrix is fed into the algorithm. In three-class H&E stained liver tissue image classification, our modified PCA algorithm achieves 74.7% accuracy with color space features. It is shown that significant classification accuracies can be achieved by using H&E stained tissue images.

We also utilized the SIFT algorithm for feature extraction. SIFT features achieve 81.4% patient classification accuracy in 'cancerous or not' classification. However, this algorithm does not produce good results in three-class classification and grading of cancerous tissue images.

In LBP implementation, we extract features using LBP algorithm around SIFT keypoints. This algorithm cannot produce meaningful results in all two-class and three-class classification cases due to the fact that H&E stained liver tissues do not have directionally distinguishing features.

We also classify H&E stained liver tissue images with modified PCA algorithm using directional feature extraction methods. Directional features achieve 86.1% patient classification accuracy in 'cancerous or not' classification. However, experimental results show that directional features do not provide distinguishing information between low-grade and high-grade cancerous tissues. Hence, these features are not useful for grading cancerous tissues.

In order to further speed up the CAD system, we develope computationally efficient versions of the modified PCA algorithm. These versions are obtained by replacing multiplication operations by multiplication-free operators in the distance calculation phase of the modified PCA algorithm. Experimental results show that these computationally efficient versions of the modified PCA algorithm can outperform the ordinary modified PCA algorithm that uses multiplication operations. The best three-class H&E stained liver tissue image classification accuracy in this thesis is 76.0% and it is achieved by multiplication-free $c4$ similarity measure (4.14) based modified PCA algorithm, which is also computationally more efficient than the ordinary modified PCA algorithm.

Bibliography

[1] P. Skaane, K. Young, and A. Skjennald, "Population-based mammography screening: Comparison of screen-film and full-field digital mammography with soft-copy readingoslo i study 1," *Radiology*, vol. 229, no. 3, pp. 877–884, 2003.

[2] M. A. Gavrielides, B. D. Gallas, P. Lenz, A. Badano, and S. M. Hewitt, "Observer variability in the interpretation of her2/neu immunohistochemical expression with unaided and computer-aided digital microscopy," *Archives of pathology & laboratory medicine*, vol. 135, no. 2, pp. 233–242, 2011.

[3] J. M. Lewin, R. E. Hendrick, C. J. DOrsi, P. K. Isaacs, L. J. Moss, A. Karellas, G. A. Sisney, C. C. Kuni, and G. R. Cutter, "Comparison of full-field digital mammography with screen-film mammography for cancer detection: Results of 4,945 paired examinations 1," *Radiology*, vol. 218, no. 3, pp. 873–880, 2001.

[4] L. Barisoni, C. C. Nast, J. C. Jennette, J. B. Hodgin, A. M. Herzenberg, K. V. Lemley, C. M. Conway, J. B. Kopp, M. Kretzler, C. Lienczewski, *et al.*, "Digital pathology evaluation in the multicenter nephrotic syndrome study network (neptune)," *Clinical Journal of the American Society of Nephrology*, vol. 8, no. 8, pp. 1449–1459, 2013.

[5] A. J. Mendez, P. G. Tahoces, M. J. Lado, M. Souto, and J. J. Vidal, "Computer-aided diagnosis: Automatic detection of malignant masses in digitized mammograms," *Medical Physics*, vol. 25, no. 6, pp. 957–964, 1998.

[6] N. M. Gürcan, Y. Yardimci, E. A. Çetin, and R. Ansari, "Automated detection and enhancement of microcalcifications in mammograms using nonlinear subband decomposition," in *Acoustics, Speech, and Signal Processing, 1997. ICASSP-97., 1997 IEEE International Conference on*, vol. 4, pp. 3069–3072, IEEE, 1997.

[7] J. Tang, R. M. Rangayyan, J. Xu, I. El Naqa, and Y. Yang, "Computer-aided detection and diagnosis of breast cancer with mammography: recent advances," *Information Technology in Biomedicine, IEEE Transactions on*, vol. 13, no. 2, pp. 236–251, 2009.

[8] A. Bozkurt, "Comparison of Multi-Scale Directional Feature Extraction Methods for Image Processing," Master's thesis, Bilkent University, 2013.

[9] M. Turk and A. Pentland, "Eigenfaces for recognition," *J. Cognitive Neuroscience*, vol. 3, pp. 71–86, Jan. 1991.

[10] M. A. Turk and A. P. Pentland, "Face recognition using eigenfaces," in *Computer Vision and Pattern Recognition, 1991. Proceedings CVPR'91., IEEE Computer Society Conference on*, pp. 586–591, IEEE, 1991.

[11] O. Oğuz, C. E. Akbaş, M. Mallah, K. Taşdemir, E. Akhan Güzelcan, C. Muenzenmayer, T. Wittenberg, A. Üner, A. E. Çetin, and R. Çetin Atalay, "Mixture of learners for cancer stem cell detection using cd13 and h and e stained images," 2016.

[12] M. K. K. Niazi, J. Hemminger, H. Kurt, G. Lozanski, and M. Gurcan, "Grading vascularity from histopathological images based on traveling salesman distance and vessel size," in *SPIE Medical Imaging*, pp. 90410C–90410C, International Society for Optics and Photonics, 2014.

[13] M. N. Gurcan and A. Madabhushi, "Medical imaging 2015: Digital pathology," in *Proc. of SPIE Vol*, vol. 9420, pp. 942001–1, 2015.

[14] M. F. A. Fauzi, M. Pennell, B. Sahiner, W. Chen, A. Shanaah, J. Hemminger, A. Gru, H. Kurt, M. Losos, A. Joehlin-Price, *et al.*, "Classification of follicular lymphoma: the effect of computer aid on pathologists grading," *BMC medical informatics and decision making*, vol. 15, no. 1, p. 1, 2015.

[15] M. Veta, J. P. Pluim, P. J. van Diest, M. Viergever, *et al.*, "Breast cancer histopathology image analysis: A review," *Biomedical Engineering, IEEE Transactions on*, vol. 61, no. 5, pp. 1400–1411, 2014.

[16] M. N. Gurcan, T. Pan, H. Shimada, and J. Saltz, "Image analysis for neuroblastoma classification: segmentation of cell nuclei," in *Engineering in Medicine and Biology Society, 2006. EMBS'06. 28th Annual International Conference of the IEEE*, pp. 4844–4847, IEEE, 2006.

[17] E. Cosatto, M. Miller, H. P. Graf, and J. S. Meyer, "Grading nuclear pleomorphism on histological micrographs," in *Pattern Recognition, 2008. ICPR 2008. 19th International Conference on*, pp. 1–4, IEEE, 2008.

[18] R. Bhagavatula, M. Fickus, W. Kelly, C. Guo, J. Ozolek, C. Castro, J. Kovačevi, *et al.*, "Automatic identification and delineation of germ layer components in h&e stained images of teratomas derived from human and nonhuman primate embryonic stem cells," in *Biomedical Imaging: From Nano to Macro, 2010 IEEE International Symposium on*, pp. 1041–1044, IEEE, 2010.

[19] S. Petushi, C. Katsinis, C. Coward, F. Garcia, and A. Tozeren, "Automated identification of microstructures on histology slides," in *Biomedical Imaging: Nano to Macro, 2004. IEEE International Symposium on*, pp. 424–427, IEEE, 2004.

[20] O. Sertel, G. Lozanski, A. Shana'ah, and M. N. Gurcan, "Computer-aided detection of centroblasts for follicular lymphoma grading using adaptive likelihood-based cell segmentation," *Biomedical Engineering, IEEE Transactions on*, vol. 57, no. 10, pp. 2613–2616, 2010.

[21] O. Sertel, U. V. Catalyurek, H. Shimada, and M. N. Gurcan, "Computer-aided prognosis of neuroblastoma: Detection of mitosis and karyorrhexis cells in digitized histological images," in *Engineering in Medicine and Biology Society, 2009. EMBC 2009. Annual International Conference of the IEEE*, pp. 1433–1436, IEEE, 2009.

[22] O. Sertel, J. Kong, G. Lozanski, U. Catalyurek, J. H. Saltz, and M. N. Gurcan, "Computerized microscopic image analysis of follicular lymphoma," in *Medical Imaging*, pp. 691535–691535, International Society for Optics and Photonics, 2008.

[23] K. Belkacem-Boussaid, M. Pennell, G. Lozanski, A. Shanaah, and M. N. Gurcan, "Computer-aided classification of centroblast cells in follicular lymphoma," *Analytical and quantitative cytology and histology/the International Academy of Cytology [and] American Society of Cytology*, vol. 32, no. 5, p. 254, 2010.

[24] D. G. Lowe, "Object recognition from local scale-invariant features," in *Computer vision, 1999. The proceedings of the seventh IEEE international conference on*, vol. 2, pp. 1150–1157, Ieee, 1999.

[25] D. G. Lowe, "Distinctive image features from scale-invariant keypoints," *International journal of computer vision*, vol. 60, no. 2, pp. 91–110, 2004.

[26] Y. Ke and R. Sukthankar, "Pca-sift: A more distinctive representation for local image descriptors," in *Computer Vision and Pattern Recognition, 2004. CVPR 2004. Proceedings of the 2004 IEEE Computer Society Conference on*, vol. 2, pp. II–506, IEEE, 2004.

[27] D. G. Lowe, "Demo software: Sift keypoint detector." `http://www.cs.ubc.ca/~lowe/keypoints/siftDemoV4.zip/`, 2005.

[28] T. Ahonen, A. Hadid, and M. Pietikainen, "Face description with local binary patterns: Application to face recognition," *Pattern Analysis and Machine Intelligence, IEEE Transactions on*, vol. 28, no. 12, pp. 2037–2041, 2006.

[29] T. Ahonen, A. Hadid, and M. Pietikäinen, "Face recognition with local binary patterns," in *Computer vision-eccv 2004*, pp. 469–481, Springer, 2004.

[30] T. Ojala, M. Pietikäinen, and D. Harwood, "A comparative study of texture measures with classification based on featured distributions," *Pattern recognition*, vol. 29, no. 1, pp. 51–59, 1996.

[31] C. Shan, S. Gong, and P. W. McOwan, "Facial expression recognition based on local binary patterns: A comprehensive study," *Image and Vision Computing*, vol. 27, no. 6, pp. 803–816, 2009.

[32] G. Zhao and M. Pietikainen, "Dynamic texture recognition using local binary patterns with an application to facial expressions," *Pattern Analysis and Machine Intelligence, IEEE Transactions on*, vol. 29, no. 6, pp. 915–928, 2007.

[33] C. E. Akbaş, A. Bozkurt, A. E. Çetin, R. Çetin Atalay, and A. Üner, "Multiplication-free neural networks," in *Signal Processing and Communications Applications Conference (SIU), 2015 23th*, pp. 2416–2418, IEEE, 2015.

[34] C. E. Akbaş, A. Bozkurt, M. T. Arslan, H. Aslanoğlu, and A. E. Çetin, "L1 norm based multiplication-free cosine similarity measures for big data analysis," in *Computational Intelligence for Multimedia Understanding (IWCIM), 2014 International Workshop on*, pp. 1–5, Nov 2014.

[35] A. Suhre, F. Keskin, T. Ersahin, R. Çetin Atalay, R. Ansari, and A. E. Çetin, "A multiplication-free framework for signal processing and applications in biomedical image analysis," in *Acoustics, Speech and Signal Processing (ICASSP), 2013 IEEE International Conference on*, pp. 1123–1127, May 2013.

[36] H. Tuna, I. Onaran, and A. E. Çetin, "Image description using a multiplier-less operator," *Signal Processing Letters, IEEE*, vol. 16, pp. 751–753, Sept 2009.

[37] O. Yorulmaz, T. C. Pearson, and A. E. Çetin, "Detection of fungal damaged popcorn using image property covariance features," *Computers and Electronics in Agriculture*, vol. 84, no. 0, pp. 47 – 52, 2012.

[38] K. Duman and A. E. Çetin, "Target detection in sar images using codifference and directional filters," 2010.

[39] Y. H. Habiboglu, O. Gunay, and A. E. Çetin, "Covariance matrix-based fire and flame detection method in video," *Machine Vision and Applications*, vol. 23, no. 6, pp. 1103–1113, 2012.

[40] J. Kleinberg and E. Tardos, "Approximation algorithms for classification problems with pairwise relationships: metric labeling and markov random fields," in *Foundations of Computer Science, 1999. 40th Annual Symposium on*, pp. 14–23, 1999.

[41] M. S. Charikar, "Similarity estimation techniques from rounding algorithms," in *Proceedings of the Thiry-fourth Annual ACM Symposium on Theory of Computing*, STOC '02, (New York, NY, USA), pp. 380–388, ACM, 2002.